DISEASES AND DISORDERS

Patient-centered connectivity-based prediction of tau pathology spread in Alzheimer's disease

Nicolai Franzmeier[1]*, Anna Dewenter[1], Lukas Frontzkowski[1], Martin Dichgans[1,2,3], Anna Rubinski[1], Julia Neitzel[1], Ruben Smith[4,5], Olof Strandberg[5], Rik Ossenkoppele[5,6], Katharina Buerger[1,3], Marco Duering[1], Oskar Hansson[5,7], Michael Ewers[1,3]*

In Alzheimer's disease (AD), the Braak staging scheme suggests a stereotypical tau spreading pattern that does, however, not capture interindividual variability in tau deposition. This complicates the prediction of tau spreading, which may become critical for defining individualized tau-PET readouts in clinical trials. Since tau is assumed to spread throughout connected regions, we used functional connectivity to improve tau spreading predictions over Braak staging methods. We included two samples with longitudinal tau-PET from controls and AD patients. Cross-sectionally, we found connectivity of tau epicenters (i.e., regions with earliest tau) to predict estimated tau spreading sequences. Longitudinally, we found tau accumulation rates to correlate with connectivity strength to patient-specific tau epicenters. A connectivity-based, patient-centered tau spreading model improved the assessment of tau accumulation rates compared to Braak stage–specific readouts and reduced sample sizes by ~40% in simulated tau-targeting interventions. Thus, connectivity-based tau spreading models may show utility in clinical trials.

INTRODUCTION

β-amyloid (Aβ) and tau pathology are hallmark pathologies of Alzheimer's disease (AD). Aβ forms extracellular plaques that accumulate in a brain-wide manner decades before symptom onset (1). In contrast, intracellular neocortical tau pathology emerges closer to symptom onset in circumscribed hotspots from where it spreads throughout the brain, ensuing neurodegeneration, cognitive decline, and, ultimately, dementia (2, 3). Postmortem examinations have shown that earliest tau pathology typically occurs in the locus coeruleus and entorhinal cortex and, subsequently, in the hippocampus, inferior temporal cortex, association cortices, and, eventually, in the primary sensorimotor and visual cortex, as summarized in the "Braak staging scheme" of progressively expanding tau pathology in AD (2, 4). The sequential emergence of tau pathology across interconnected brain regions has fostered the idea that tau pathology spreads "prion like" across connected neurons (5, 6). In cultured neurons and tau transgenic mice, intracellular tau pathology is propagated transsynaptically from neuron to neuron (5, 6), possibly in a neural activity–dependent manner (7), suggesting that tau pathology may spread along connections between actively communicating brain regions. In a translational approach, several neuroimaging studies in humans have demonstrated that functional magnetic resonance imaging (fMRI)–assessed functional connectivity between brain regions is predictive of the spatial pattern of tau pathology, as assessed by positron emission tomography (PET): First, the spatial covariance patterns of tau-PET uptake resemble functional brain network topology, indicative of correlated tau accumulation

within functionally connected brain networks (8, 9). Second, brain regions that are highly interconnected with the rest of the brain, i.e., so-called hubs, show relatively high tau-PET levels, consistent with the idea that such regions are more likely to receive pathological tau species from remote regions (10). Third, functionally interconnected brain regions in patients with AD exhibit similar tau-PET uptake (11) and longitudinally assessed tau accumulation rates (12). We further showed that the levels of future tau accumulation in a given brain region can be predicted by the levels of baseline tau pathology in connected regions (12). Together, these findings provide converging evidence for a positive association between brain connectivity and the accumulation of tau pathology.

While tau spreading in AD is classically argued to follow a stereotypical spatiotemporal pattern summarized by the Braak staging scheme, postmortem and in vivo tau-PET studies have uncovered substantial interindividual heterogeneity in tau deposition patterns with notable deviations from the Braak scheme (13–16). Spatial variants of tau deposition include those, among others, that are asymmetric between hemispheres, posterior dominant, limbic predominant, or hippocampal sparing (13–16). The spatial heterogeneity in tau deposition patterns is not primarily driven by different disease severity levels but corresponds to different clinical profiles including posterior cortical atrophy (with occipital tau deposition), nonamnestic AD (with hippocampus sparing tau), and logopenic primary progressive aphasia (with left-dominant temporoparietal tau deposition) (14, 16–18). Longitudinal tau-PET studies further showed that spatial tau accumulation patterns show substantial interindividual variability regardless of clinical stage that can deviate substantially from the Braak staging scheme (19–23). This interindividual heterogeneity in tau spreading patterns poses challenges to accurately predict tau progression at the individual level based on established tau spreading schemes (19–23). Subject-level prediction of future tau spreading might, however, become critical to define individualized tau-PET readouts for clinical trials using tau-PET. Individualized tau-PET readouts can help enhance the sensitivity to detect treatment effects and help reduce the number of patients included into these trials. This is of high clinical importance since

[1]Institute for Stroke and Dementia Research (ISD), University Hospital, LMU Munich, Munich, Germany. [2]Munich Cluster for Systems Neurology, Munich, Germany. [3]German Center for Neurodegenerative Diseases (DZNE), Munich, Germany. [4]Department of Neurology, Skåne University Hospital, Lund, Sweden. [5]Clinical Memory Research Unit, Department of Clinical Sciences Malmö, Lund University, Lund, Sweden. [6]Alzheimer Center Amsterdam, Department of Neurology, Amsterdam Neuroscience, Vrije Universiteit Amsterdam, Amsterdam UMC, Amsterdam, Netherlands. [7]Memory Clinic, Skåne University Hospital, Malmö, Sweden.
*Corresponding author. Email: nicolai.franzmeier@med.uni-muenchen.de (N.F.); michael.ewers@med.uni-muenchen.de (M.E.)

targeting tau is gaining increasing attention as a treatment strategy against AD, especially in light of the numerous failed anti-amyloid trials (*24*). Given the close link between the localization of tau pathology and the occurrence of cognitive domain–specific dementia symptoms (*25, 26*), the identification of brain regions in which tau will subsequently accumulate may further aid in prognostication and planning of personalized patient management.

Against this background, we aimed to predict future spreading patterns of tau pathology in a given patient with AD based on (i) the individual identification of regions with high tau-PET uptake at baseline (henceforth termed as "tau epicenter") and (ii) fMRI-assessed connectivity of the tau epicenter. We hypothesized that tau accumulation rates would be fastest in regions closely connected to the epicenter and slowest in regions only weakly connected to the epicenter. In other words, we expected a gradient of tau accumulation from tau epicenters throughout the brain. Such a connectivity-based prediction model would allow for a patient-tailored prediction of regional spreading of tau pathology, going beyond a general tau staging scheme such as the Braak staging to predict the spread of tau pathology as the disease progresses. Thus, the overall aim of this study was to establish and validate a connectivity-based prediction model of patient-specific tau spreading.

To address this, we included ^{18}F-flortaucipir tau-PET (i.e., AV1451) data from two independent samples of patients across the Alzheimer's continuum. The discovery sample included 213 amyloid-positive subjects (106 with longitudinal tau-PET data) and 231 controls from the Alzheimer's Disease Neuroimaging Initiative (ADNI). The validation sample included amyloid-positive subjects (*n* = 41) and amyloid-negative controls (*n* = 16) from the Swedish BioFINDER cohort (all with longitudinal tau-PET data). For functional connectivity, we used a normative connectivity template (i.e., based on resting-state fMRI data of 1000 participants of the human connectome project) to develop a tau spreading model that is broadly applicable to clinically acquired tau-PET data, without the necessity of high-quality subject-level fMRI data, which can be difficult to obtain in clinical settings. Using cross-sectional tau-PET data, we first estimated tau spreading sequences across the AD continuum and show in both samples that the AD-typical sequence of PET-assessed tau accumulation largely follows the connectivity pattern of regions with earliest tau, i.e., tau epicenters located in the inferior temporal lobe. To replicate this association in spatial subtypes of tau deposition with heterogeneous tau spreading patterns, we divided the large cross-sectional ADNI discovery dataset of 213 amyloid-positive subjects into spatially defined tau-PET subtypes using independent component analysis (ICA) (*27*). We show for each spatial tau-PET subtype that cross-sectionally estimated tau spreading sequences follow the connectivity pattern of tau epicenters that are spatially variable across subtypes. This finding suggests that heterogeneous tau spreading patterns can be explained by variable tau epicenters (i.e., starting sites of tau pathology) and subsequent spread throughout the connected regions. Last, to address our main aim, we tested the association between epicenter connectivity and future tau accumulation at the individual level by using longitudinal tau-PET data of amyloid-positive subjects: In both samples, we show that the connectivity pattern of a given subjects' tau epicenter predicts future tau accumulation patterns, with the fastest tau accumulation in regions strongly connected to the epicenters versus slowest tau accumulation in regions only weakly connected to the epicenters. This confirms our hypothesis that individual tau spread-

ing patterns are to a high degree explained by connectivity patterns of tau epicenters. Informed by this, we establish an independently validated and subject-specific prediction model of future tau spreading: This model combines subject-level baseline tau-PET and normative connectivity data to determine a subject-tailored region of interest (ROI) with the highest likelihood of future tau accumulation. We show that longitudinal tau accumulation in the connectivity-based, patient-tailored ROI is significantly higher than tau accumulation in predefined regions based on the Braak staging scheme. Together, individualized connectivity-based prediction of tau spreading allows more sensitive assessments of tau changes than the stereotypic Braak staging scheme that is agnostic to subject-specific tau epicenters and spreading patterns. Last, we show that the proposed individualized spreading model can help increase the sensitivity to detect tau accumulation and reduce sample sizes for clinical trials using tau-PET end points.

RESULTS

As a discovery sample, we included 444 subjects with available baseline AV1451 tau-PET, AV45 amyloid-PET, and T1 structural MRI from the ADNI database. To cover the Alzheimer's continuum (defined by abnormal amyloid-PET, Aβ$^+$), the sample encompassed 117 cognitively normal (CN) Aβ$^+$, 85 mild cognitively impaired (MCI) Aβ$^+$, and 11 patients with AD dementia (i.e., Aβ$^+$). Two hundred thirty-one CN Aβ$^−$ participants served as a control group. For a total of 106 Aβ$^+$ participants (i.e., 61 CN Aβ$^+$, 40 MCI Aβ$^+$, and 5 AD dementia), longitudinal AV1451 tau-PET with an average follow-up time of 1.58 ± 0.75 years was available. As an independent validation sample, we used cross-sectional and longitudinal AV1451 tau-PET data from the BioFINDER cohort, including 16 CN Aβ$^−$ controls and 41 participants covering the Alzheimer's continuum (i.e., 16 CN Aβ$^+$, 7 MCI Aβ$^+$, and 18 Aβ$^+$ patients with AD dementia) with ~1.92 ± 0.36 years of tau-PET follow-up. Baseline characteristics of each sample are summarized in Table 1. A flow chart illustrating study design and analyses is provided in fig. S1.

Transforming AV1451 tau-PET SUVRs to tau positivity probabilities

Before addressing our major aims, we transformed AV1451 tau-PET standardized uptake value ratio (SUVR) values (i.e., intensity normalized to the inferior cerebellar gray) to regional tau positivity probabilities, i.e., the probability to stem from the population of pathologically increased tau-PET values, using a pre-established approach (*28*). The rationale is based on previous work describing considerable off-target binding of the AV1451 tracer, resulting in mixed on-target and off-target signal across the brain and thus false positives, which may significantly bias the modeling of tau spreading (*29, 30*). To minimize the influence of AV1451 off-target binding in our analyses, we parcellated the brain into 200 neocortical brain regions included in a standard brain atlas (Fig. 1A) (*31*) and applied for each ROI a two-component Gaussian mixture model to separate the underlying distributions of off-target (i.e., a normal distribution with a low mean SUVR) versus on-target binding (i.e., a skewed distribution with a higher mean SUVR), as illustrated in Fig. 1B (see Materials and Methods for a more in-depth description). For each individual and ROI, we then assessed the probability of belonging to the "on-target binding" distribution, henceforth referred to as tau positivity probability. Average tau positivity maps

Table 1. Sample characteristic-s. ADAS, Alzheimer's Disease Assessment Scale.

ADNI	CN-Aβ⁻ (n = 231)	CN-Aβ⁺ (n = 117)	MCI-Aβ⁺ (n = 85)	AD dementia (n = 11)	P value
Age	72.76 ± 6.98*,†	76.91 ± 7.49‡	75.94 ± 7.67‡	74.36 ± 10.23	<0.001
Sex (m/f)	93/138	47/70	49/36	6/5	0.030
Education (M/SD)	16.82 ± 2.41†	16.44 ± 2.6	15.88 ± 2.64‡	16 ± 2.05	0.025
MMSE (M/SD)					
ADAS global (M/SD)	12.27 ± 4.55†,§	13.61 ± 5.41†,§	23.18 ± 11*,‡,§	32.21 ± 8.26*,†,‡	<0.001
Mean tau-PET follow-up time in years (M/SD)[1]	NA	1.61 ± 0.79	1.56 ± 0.71	1.44 ± 0.72	0.871
BioFINDER	**CN-Aβ⁻ (n = 16)**	**CN-Aβ⁺ (n = 16)**	**MCI-Aβ⁺ (n = 7)**	**AD dementia (n = 18)**	
Age	73.88 (5.32)	75.44 (6.09)	72.71 (6.63)	69.83 (10.48)	0.192
Sex (m/f)	10/6	6/10	2/5	11/7	0.245
Education (M/SD)	12.59 (4.06)	10.56 (3.22)	11.14 (2.67)	13.44 (3.26)	0.097
MMSE (M/SD)	29 (1.1)§	29.31 (1.08)§	25.57 (2.94)	22.06 (5.17)*,‡	<0.001
ADAS-delayed recall (M/SD)	1.81 (1.47)†,§	2.31 (1.49)†,§	6.17 (2.4)	7.62 (2.45)*,‡	<0.001
ApoE ε4 status (pos/neg)	0/16	10/6	4/3	11/7	<0.001
Global flutemetamol SUVR	0.52 (0.03)*,†,§	0.77 (0.12)‡,§	0.84 (0.14)‡	0.97 (0.15)*,‡	<0.001
Mean tau-PET follow-up time in years (M/SD)	2.03 (0.47)	1.91 (0.32)	1.82 (0.12)	1.97 (0.34)	0.484

1 = subsample of 61 CN Aβ⁺, 40 MCI Aβ⁺, and 5 AD dementia. *significantly different from CN Aβ⁺, † significantly different from MCI Aβ⁺, ‡significantly different from CN Aβ⁻, §significantly different from AD dementia.

for each diagnostic group and sample (i.e., ADNI and BioFINDER) at baseline are displayed in Fig. 1C, showing increasing tau positivity probabilities across the Alzheimer's continuum.

Cross-sectional estimation of tau spreading sequences in Aβ⁺

To model the AD-typical spatiotemporal sequence of tau spreading, we used a previously developed approach including the frequency-based ranking of tau positivity applied to cross-sectional PET data (28). The estimation of tau spreading sequences on cross-sectional data is illustrated in Fig. 1D and described in detail in Materials and Methods. This analysis is based on the assumption that regions that develop abnormal tau early in AD should show abnormal tau levels across many Aβ⁺ subjects, whereas regions that develop abnormal tau relatively late in AD should show abnormal tau levels in relatively few Aβ⁺ subjects. We applied this approach to the cross-sectional tau positivity maps of the 213 Aβ⁺ ADNI subjects (discovery sample) and 41 Aβ⁺ BioFINDER subjects (validation sample) to determine tau spreading matrices for each sample (Fig. 2, A and E for ADNI and BioFINDER, respectively). The estimated spatiotemporal sequences of tau spreading (see surface renderings in Fig. 2, B and F for ADNI and BioFINDER, respectively) were highly consistent across ADNI and BioFINDER (spatial correlation: $r = 0.78$, $R^2 = 0.61$, $P < 0.001$), suggesting that the group average spatial pattern of tau spreading is consistent across studies. In both samples, earliest tau positivity was found in inferior temporal regions, followed by association cortices of the parietal and frontal lobe and lastly by unimodal sensorimotor and visual regions (see Fig. 2, B and F). Still,

there is considerable heterogeneity across subjects, as shown in the tau spreading matrices (Fig. 2, A and E), i.e., some subjects show high tau levels in brain regions that typically develop tau late in the estimated tau spreading sequence, while early or intermediate tau regions are still spared.

In Aβ⁺, estimated tau spreading sequences follow the connectivity pattern of tau epicenters

We next tested whether the AD-typical sequence in which brain regions become tau positive can be predicted by the connectivity pattern of tau epicenters (i.e., brain regions in which tau emerges first). Using the cross-sectionally estimated tau spreading sequences (Fig. 2, B and F), we determined for each, both the discovery and the validation sample, the 10% ROIs as "epicenters" in which tau accumulates first, as estimated from the above described analysis (see green box in Fig. 2, A and E and green outlined regions covering mostly the bilateral inferior temporal cortex in Fig. 2, B and F). To determine functional connectivity, we used the same 200 ROI parcellation shown in Fig. 1A to assess a group-average 200 × 200 ROI of weighted functional connectivity matrix based on preprocessed resting-state fMRI data from 1000 healthy individuals of the human connectome project (Fig. 2I). This 200 × 200 connectivity template was density thresholded at 30% (Fig. 2J; i.e., 30% of the strongest positive connections were retained) to remove spurious connections and transformed to connectivity-based distance (Fig. 2K). Connectivity-based distance is inversely related to connectivity strength ($r = -0.87$, $P < 0.001$; Fig. 2L) and describes the path length between each ROI pair, i.e., strongly connected ROIs are "close," while weakly or indirectly
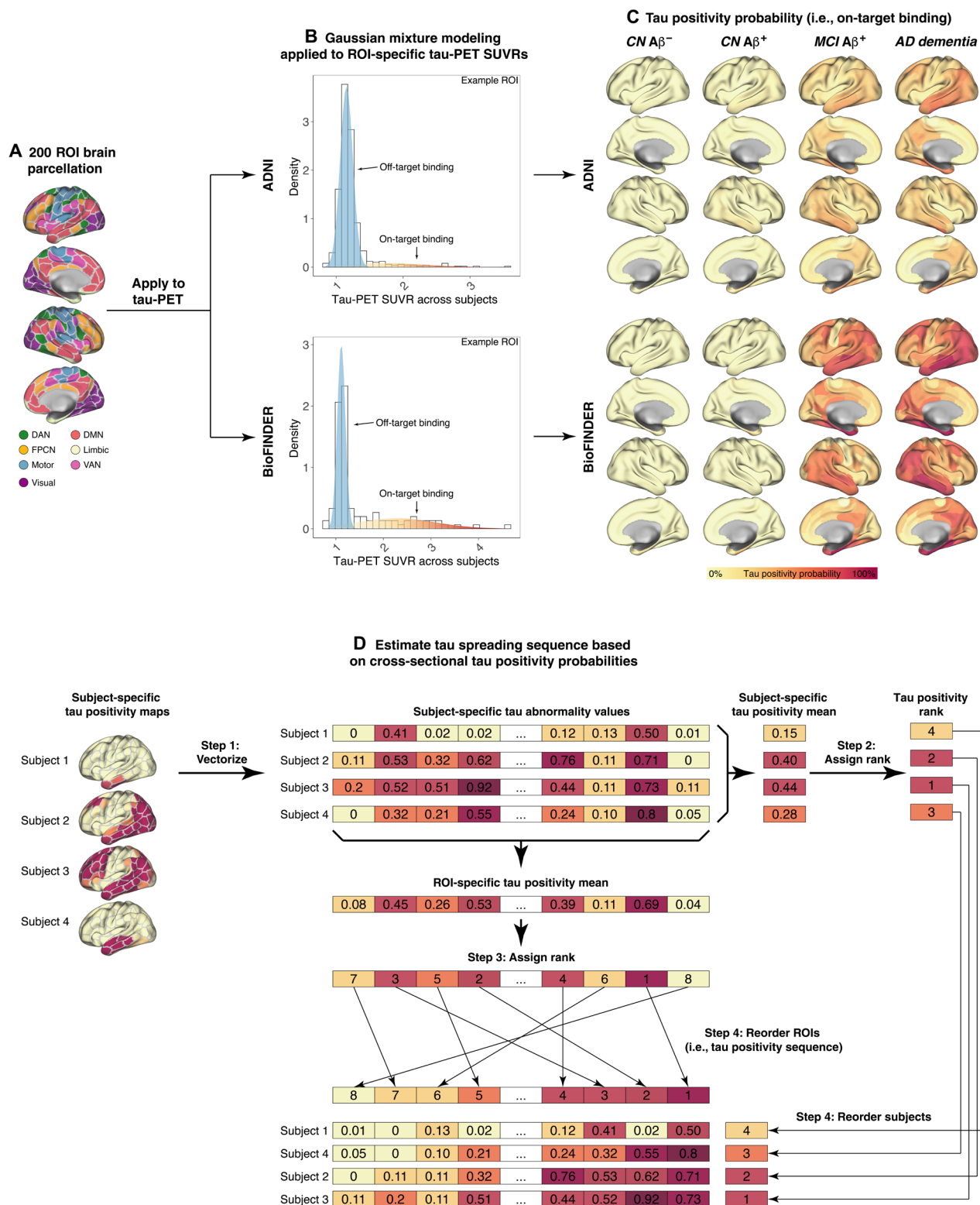
Fig. 1. Assessment of tau positivity probabilities and tau spreading sequences. Preprocessed voxel-wise tau-PET SUVR images were parcellated in 200 cortical ROIs (**A**). Two-component Gaussian mixture modeling was applied to ROI-specific tau-PET data (**B**) in order separate off target from target binding to transform tau-PET SUVRs to tau positivity probabilities (**C**). Cross-sectional tau positivity probabilities were used to estimate spatiotemporal sequences of tau spreading (**D**). Specifically, subject- and ROI-specific tau positivity scores were concatenated in a 2D (two-dimensional) matrix (rows, subjects; columns, ROIs), which was subsequently rank ordered by row sums and column sums. The tau spreading sequence was determined on the basis of the rank order of ROIs. DAN, Dorsal Attention Network; FPCN, Fronto-Parietal Control Network; DMN, Default-Mode Network; VAN, Ventral Attention Network.
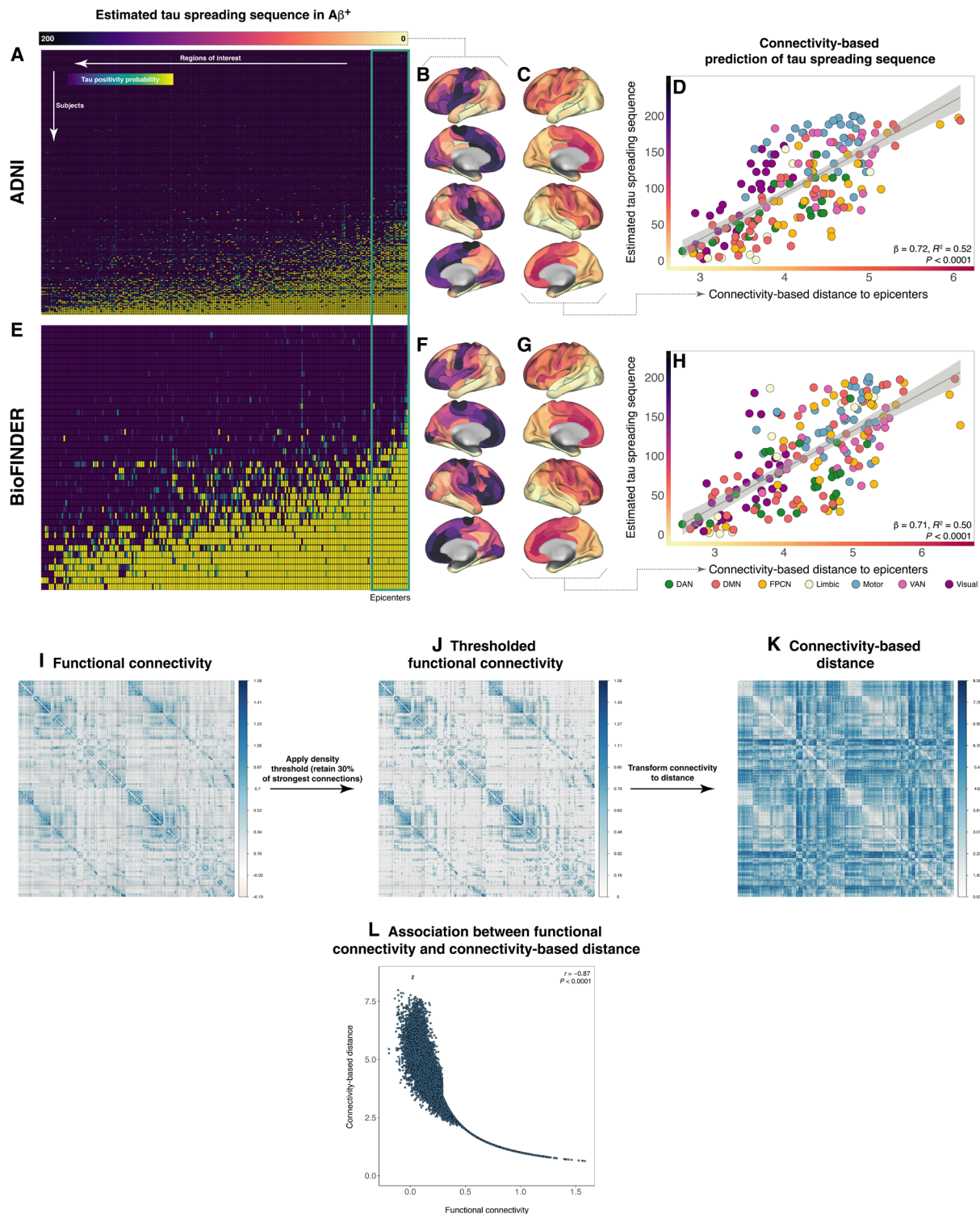
Fig. 2. Epicenter connectivity versus estimated tau spreading sequences. Tau positivity matrices for both Aβ+ subjects of the ADNI (**A**) and BioFINDER (**E**) were used to estimate tau spreading sequences for each sample. Blue colors indicate low tau positivity probabilities, while green-yellow colors indicate high tau positivity probabilities (**B** and **F**). Within each sample, tau epicenters were defined as those 10% of ROIs with earliest tau positivity [i.e., green box in (A) and (E); green outline in (B), (F), (C), and (G)]. Seed-based connectivity of the epicenters was determined on the basis of resting-state fMRI data from 1000 subjects of the human connectome project and transformed to connectivity-based distance (**C** and **G**). Scatterplots illustrate the association between connectivity-based distance to the epicenters and the tau positivity sequences for both ADNI (**D**) and BioFINDER (**H**). Using the 200 ROI brain parcellation shown in Fig. 1A, resting-state fMRI functional connectivity was assessed on 1000 subjects of the human connectome project. The resulting group-average connectivity matrix (**I**) was subsequently density thresholded to remove spurious connections (**J**) and transformed to connectivity-based distance (**K**), which is inversely related to functional connectivity (**L**).
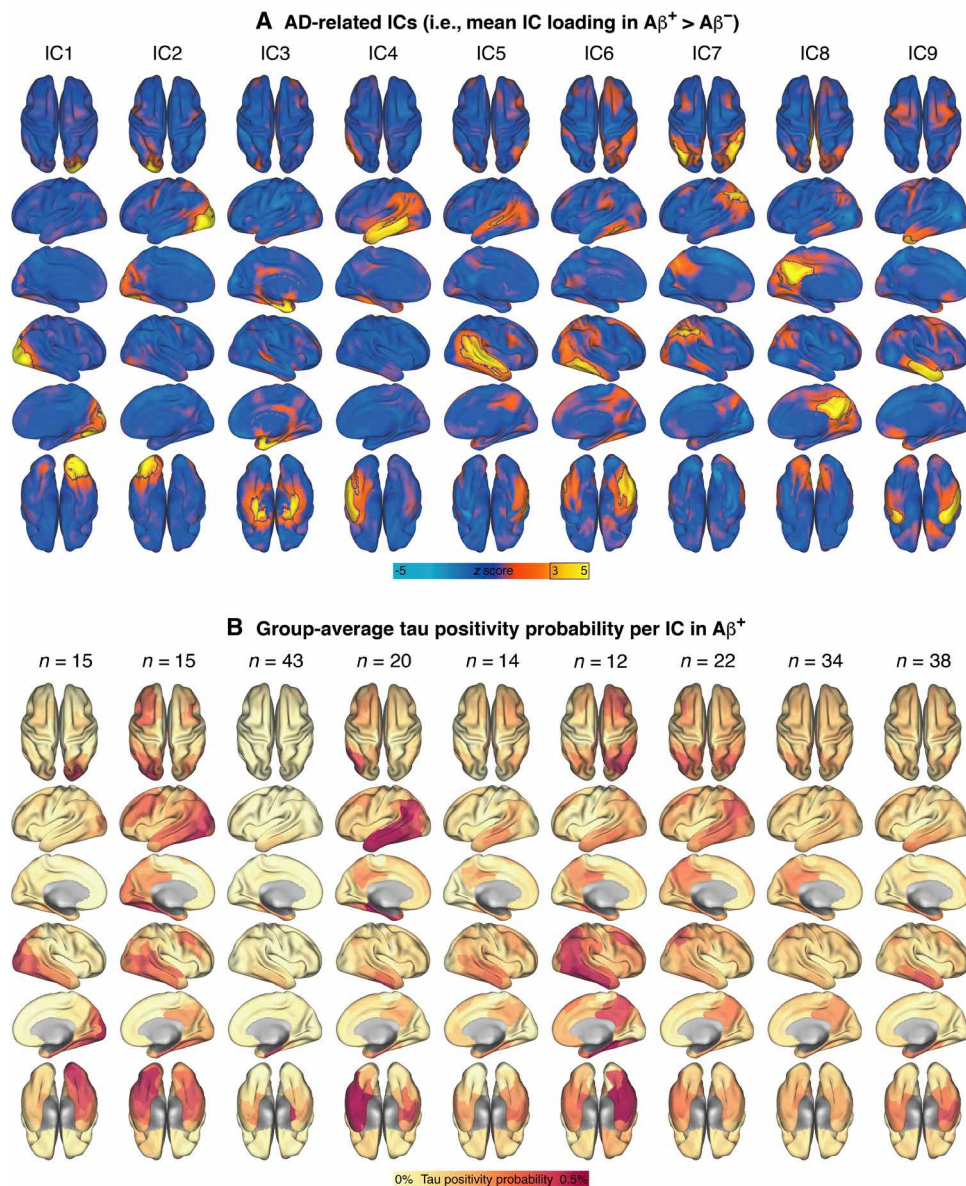
ICA-based assessment of tau subtypes in ADNI

Fig. 3. ICA-based assessment of tau subtypes in ADNI. ICA was applied to voxel-wise tau-PET SUVR data from the ADNI sample to determine spatial subtypes of tau deposition. Mean independent component (IC) loadings of 23 ICs were compared between Aβ+ and Aβ− subjects. Components were labeled as AD-related whether mean IC loadings were significantly higher in Aβ+ compared to Aβ− using two-sample t tests (α level = 0.001). Z scaled IC maps of the nine AD-related components are shown in (**A**). Aβ+ were assigned to AD-related ICs on the basis of highest IC loadings. Surface renderings of IC-average tau positivity probabilities across Aβ+ subjects are shown in (**B**).

connected ROIs are "distant." We then determined the mean connectivity-based distance for the tau epicenters derived from ADNI and BioFINDER (Fig. 2, C and G), which was used as a predictor of the estimated tau spreading sequence using linear regression. As hypothesized, we found that connectivity-based distance of the epicenters was strongly associated with the estimated tau spreading sequence in the ADNI discovery sample (β = 0.72, R^2 = 0.52, $P < 0.0001$; Fig. 2D) and the BioFINDER validation sample (β = 0.71, R^2 = 0.50, $P < 0.0001$; Fig. 2H). This association remained consistent when additionally controlling for Euclidean distance between ROIs

(ADNI: β = 0.78, R^2 = 0.61, $P < 0.001$; BioFINDER: β = 0.71, R^2 = 0.50, $P < 0.0001$), suggesting that the estimated tau spreading sequence indeed primarily follows the connectivity pattern of the tau epicenters.

To test whether thresholding the connectivity matrix at densities other than 30% drove our results, we reanalyzed the data altering the density threshold between 10 and 50%, yielding highly consistent results with our main analysis (table S1). Similarly, using 5 to 20% of ROIs with earliest tau positivity as epicenters did not change the overall result pattern (table S1). We further tested whether restricting the connectivity matrix to ROI pairs with an underlying structural

connection (assessed via diffusion imaging in 1000 human connectome project subjects; see Materials and Methods) improved the prediction of the estimated tau spreading sequence. When restricting the functional connectivity matrix to ROI pairs with an underlying structural connection at various probability thresholds, results remained consistent, but prediction accuracy did not improve (see table S2). Together, these findings confirm our hypothesis that the AD-typical tau spreading sequence follows the tau epicenters' functional connectivity pattern.

Modeling heterogeneity in tau spreading patterns
Next, we tested whether the connectivity-based prediction of tau spreading generalizes toward heterogeneous tau patterns that may deviate from the stereotypical "Braak-like" tau spreading pattern. To this end, we asked whether subjects can be meaningfully grouped into distinct spatial subtypes according to spatial tau-PET patterns. We then asked whether spatial tau subtypes are characterized by variable epicenters and whether the sequence of tau spreading follows the connectivity of subtype-specific epicenters. Thus, we assessed (i) whether the large $A\beta^+$ group of the ADNI discovery sample includes AD-specific subgroups with discriminable spatial patterns of tau-PET and (ii) whether connectivity patterns of subgroup-specific tau epicenters predict the estimated tau spreading sequences within each subgroup better than the tau spreading sequence estimated on the whole $A\beta^+$ group. To identify spatial tau-PET subtypes in a data-driven manner, we applied ICA to the cross-sectional tau-PET SUVR data from the ADNI discovery sample ($n = 444$). Note that this analysis was restricted to ADNI because of the large enough sample that allowed deriving meaningfully sized subgroups. We specifically used voxel-wise tau-PET SUVR maps rather than tau positivity probabilities at this stage to use the capability of ICA to separate noise components (i.e., off-target binding) from target binding components. Applied to cross-sectional data of the 444 ADNI subjects, the ICA identified 23 independent components (ICs), as determined by the minimum description length algorithm. To identify AD-related higher tau-PET uptake (27), we compared component loadings between $A\beta^+$ and $A\beta^-$ subjects using two-sample t tests, yielding 9 of 23 components with significant higher loadings in $A\beta^+$ versus $A\beta^-$ (i.e., $P < 0.001$). Higher loading in $A\beta^+$ than $A\beta^-$ suggests that these nine components include AD-related tau-PET signal. On the basis of maximum component loadings, $A\beta^+$ subjects were assigned to one of the nine AD-related components (see Fig. 3A for z scaled IC maps) after which we mapped group-average tau positivity maps across the 200 ROI parcellation for each IC (Fig. 3B). As expected, we found heterogeneous tau patterns across ICs: We found ICs with predominantly right (IC1) or left (IC2) occipitotemporal tau positivity, with predominant inferior temporal tau positivity (IC3 and IC9), with lateralized left (IC4) or right (IC5 and IC6) temporoparietal tau positivity, as well as predominantly lateral (IC7) and medial (IC8) parietal tau-PET positivity. Similar to the approach applied previously in the whole $A\beta^+$ group, we next (i) determined the IC-specific tau spreading matrices for the cross-sectional estimation of subtype-specific tau spreading sequences (methods illustrated in Fig. 1D), (ii) derived IC-specific epicenters (i.e., the 10% of ROIs showing earliest tau positivity), and (iii) tested for each IC whether connectivity-based distance of the epicenters predicted the IC-specific tau spreading sequence. The estimated IC-specific tau spreading sequences are shown in Fig. 4, A and B. We found for each IC that the estimated

tau spreading sequence was associated with connectivity-based distance of the epicenters ($\beta = 0.43$ to 0.70, all $P < 0.0001$; see Fig. 4C), independent of additionally controlling for Euclidean distance, or altering the connectivity threshold between 10 and 50%. The predictive accuracy (i.e., R^2) of epicenter connectivity for the estimated tau positivity sequence was significantly higher ($P < 0.001$) between IC-specific tau spreading sequences and subject-level tau positivity maps (fig. S2) compared to whole-group tau spreading sequences and subject-level tau positivity maps. This suggests that IC-specific estimates of more heterogeneous tau spreading sequences better explain subject level tau deposition patterns than the Braak-like tau spreading sequences estimated on the whole $A\beta^+$ group. To further illustrate IC-specific tau spreading patterns, we computed mean tau positivity within sliding windows applied to tau positivity maps from subjects with lowest to highest overall tau positivity (see Fig. 5A). The sliding window maps illustrate within each IC that tau abnormality starts in circumscribed epicenters with subsequent spread throughout the brain (Fig. 5, B to J). When assessing the distribution of epicenters across the nine ICs, we found that inferior temporal regions were commonly included as epicenters across most ICs, whereas superior temporal, occipital, parietal, and frontal ROIs were rather specific for a given IC (fig. S3). Together, these findings support the view that tau epicenters are spatially heterogeneous, where the connectivity pattern of the respective tau epicenters predicts the spread of tau.

Modeling subject-specific longitudinal tau spreading
Last, we tested whether the association between connectivity and cross-sectionally estimated tau spreading sequences can be confirmed on the individual level by longitudinal modeling of subject-level tau-PET spreading. To this end, we used longitudinal tau-PET data from 106 $A\beta^+$ ADNI (i.e., discovery sample) and 41 $A\beta^+$ BioFINDER subjects (i.e., validation sample). We hypothesized that rates of tau accumulation should be highest in those regions that are in close connectivity-based proximity to subject-specific epicenters versus lowest in regions that are in far connectivity-based distance to the epicenters (see Fig. 6A). To test this, we determined each subjects' tau epicenter at baseline, defined as ROIs showing at least >30% tau positivity probability (altering the probability threshold between 20 and 50% did not change the result pattern). Subjects without evidence of significant tau pathology at baseline (i.e., where none of the 200 ROIs surpassed a tau positivity probability threshold of >30%) were excluded from further analyses, leaving a total of 57 out of 106 $A\beta^+$ subjects from the ADNI discovery sample and 33 out of 41 $A\beta^+$ subjects from the BioFINDER validation sample. For each remaining subject, we then used the functional connectivity template to determine connectivity-based distance of each ROI to the subject-specific epicenters and grouped the ROIs (except for the epicenters themselves) into nonoverlapping quartiles on the basis of their connectivity-based distance to the epicenter (i.e., Q1 is closest to the epicenter versus Q4 is most distant to the epicenter, see Fig. 6A; note that Q1 to Q4 ROIs were determined for each subject individually). Across ROIs within each quartile, we then determined the average change in tau positivity from baseline to follow-up. We found a gradient of tau accumulation from Q1 to Q4, where tau changes in Q1 (i.e., 25% of ROIs that are most closely connected to the epicenter) were significantly higher than those in the epicenter itself (ADNI: Cohens $d = 0.48$, $P = 0.003$; BioFINDER, Cohens $d = 0.78$, $P = 0.0016$) and significantly higher than in the
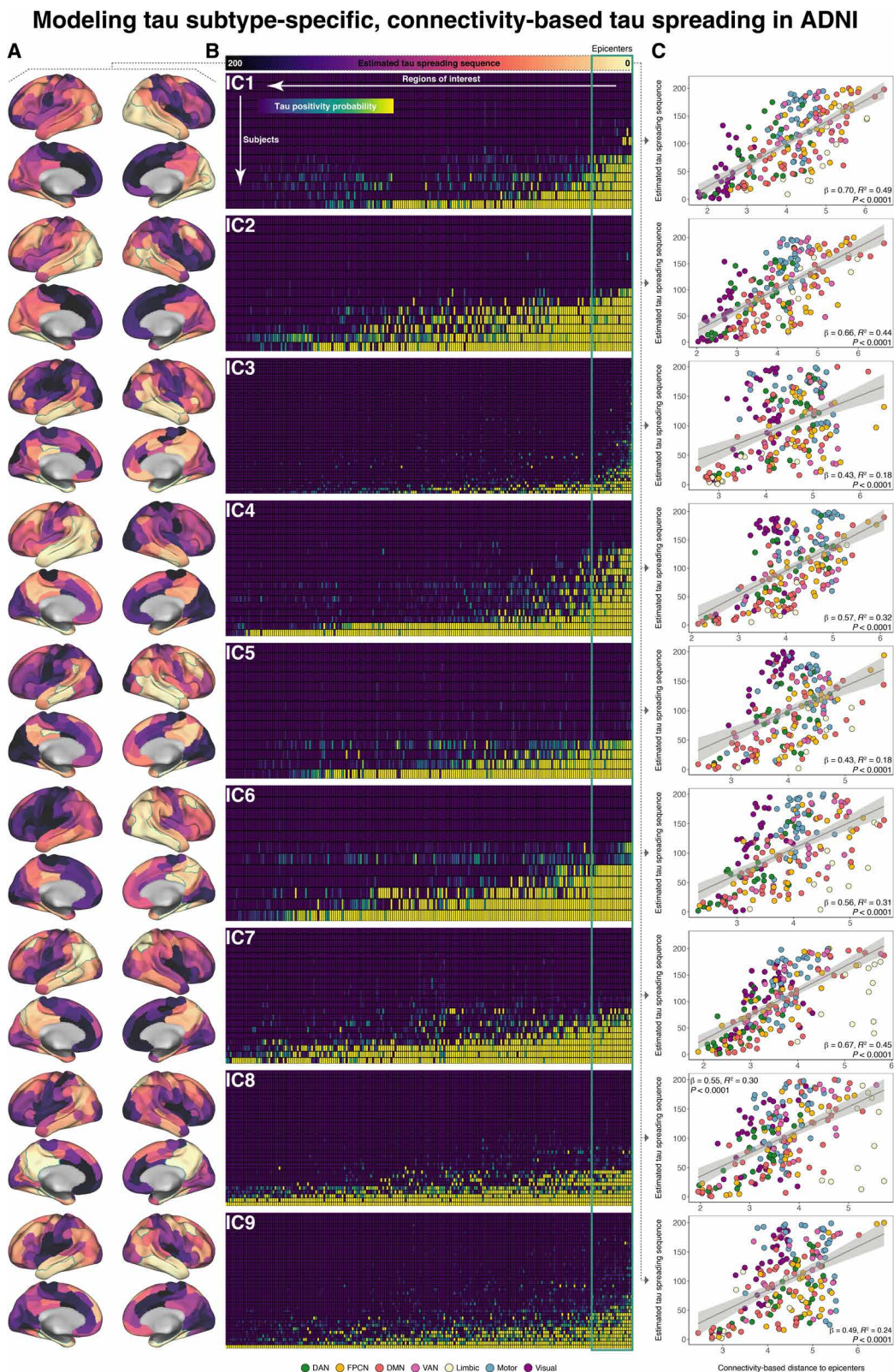
Fig. 4. Modeling tau subtype-specific, connectivity-based tau spreading in ADNI. Estimated tau spreading sequences and their association with epicenter connectivity across IC-defined tau subtypes in ADNI. (**A**) Surface maps of the estimated tau spreading sequences for each IC that were assessed on tau positivity matrices (**B**). (**C**) Association of connectivity-based distance of IC-specific epicenters [i.e., green box in (B) and green outline in (A)] and IC-specific estimated tau spreading sequences. The methodological framework of these analyses is described in Figs. 1 and 2.
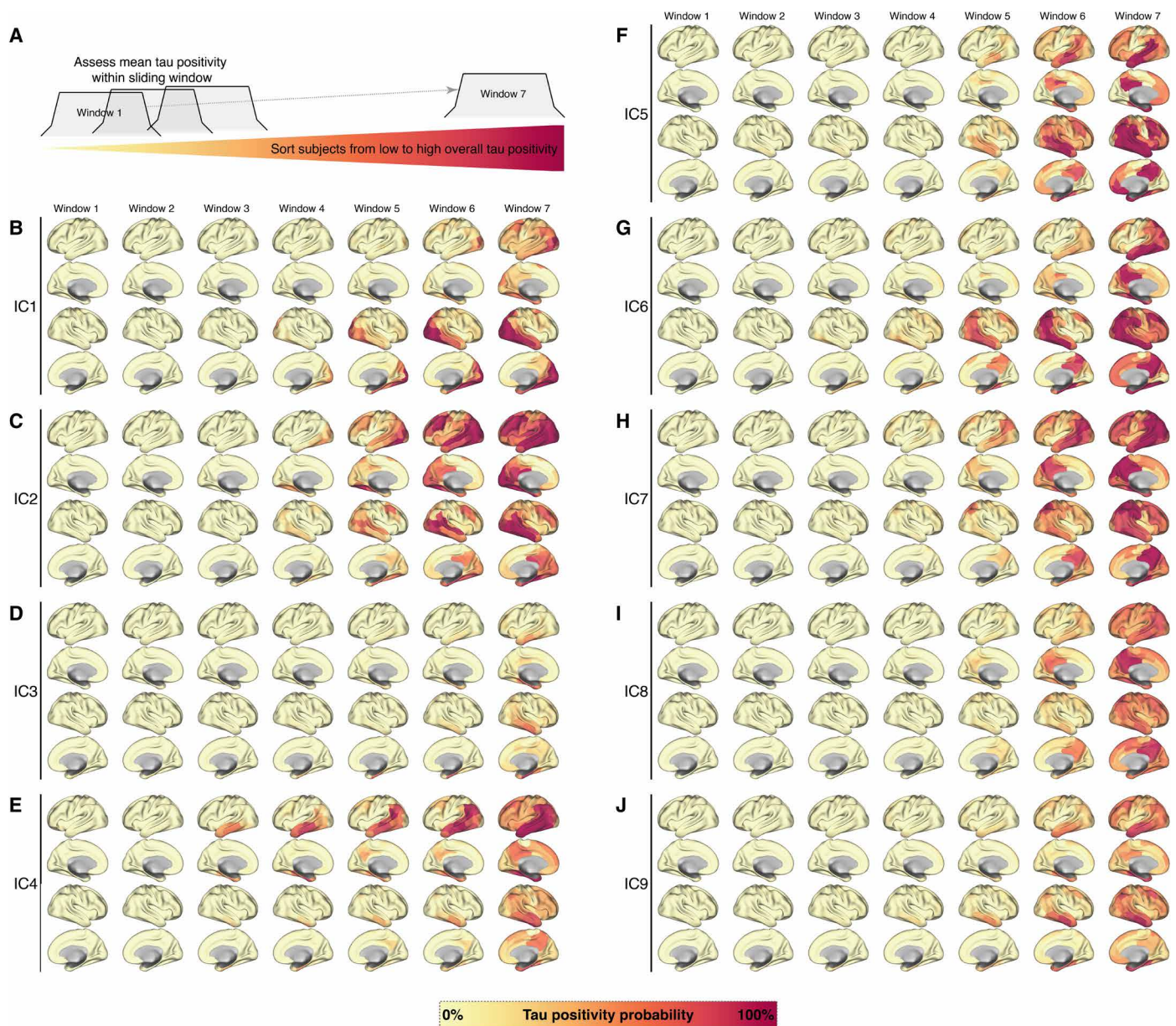
Fig. 5. Illustration of heterogeneous tau spreading patterns in tau subtypes. Sliding window analyses on tau positivity probabilities to illustrate the spatial patterns of tau accumulation across IC-defined spatial subgroups. Subjects within each IC were sorted on the basis of overall tau positivity probability (i.e., averaged across all 200 ROIs). Sliding window analysis was applied to sorted subjects (**A**) to illustrate spatial tau spreading patterns for each IC (**B** to **J**).

other quartiles, i.e., in regions that are less strongly connected to the epicenter (ADNI: Q1 versus Q2/3/4, Cohens d = 0.28/0.44/0.51, all P < 0.002; see Fig. 6B; BioFINDER: Q1 versus Q2/3/4, Cohens d = 0.35/0.41/0.46, all P < 0.001; see Fig. 6C). Results remained consistent (all P < 0.005) when controlling the analyses for mean Euclidean distance of Q1 to 4 ROIs to the epicenter. This suggests that tau accumulation is strongest in those brain regions that are functionally closely connected to the epicenters (i.e., Q1). In addition, we compared tau accumulation in Q1 with tau accumulation in Braak stage–specific ROIs (see Fig. 6F), whole-brain, or a temporal meta-ROI (i.e., Braak stage 1, 3, and 4) (*32*), which are commonly used to stage tau-PET (*3*). Using paired Wilcoxon tests, we found

that longitudinal tau changes in Q1 were significantly higher than in ROIs for Braak 1 (ADNI/BioFINDER: P = 0.022/0.019, Cohens d = 0.42/0.65), Braak 3 (ADNI/BioFINDER: P < 0.001/0.001, Cohens d = 0.57/0.82), Braak 4 (ADNI/BioFINDER: P < 0.001/0.001, Cohens d = 0.56/0.72), Braak 5 (ADNI/BioFINDER: P < 0.001/0.001, Cohens d = 0.51/0.71), and Braak 6 (ADNI/BioFINDER: P < 0.001/0.001, Cohens d = 0.67/0.55), temporal meta-ROI (ADNI/BioFINDER: P < 0.001/0.001, Cohens d = 0.55/0.82), or in the whole-brain gray matter (ADNI/BioFINDER: P < 0.001/0.001, Cohens d = 0.56/0.66). Results are summarized in Fig. 6 (D and E). These findings suggest that longitudinal tau change in the Q1 ROI (i.e., which is determined for each subject individually on template-based connectivity to the
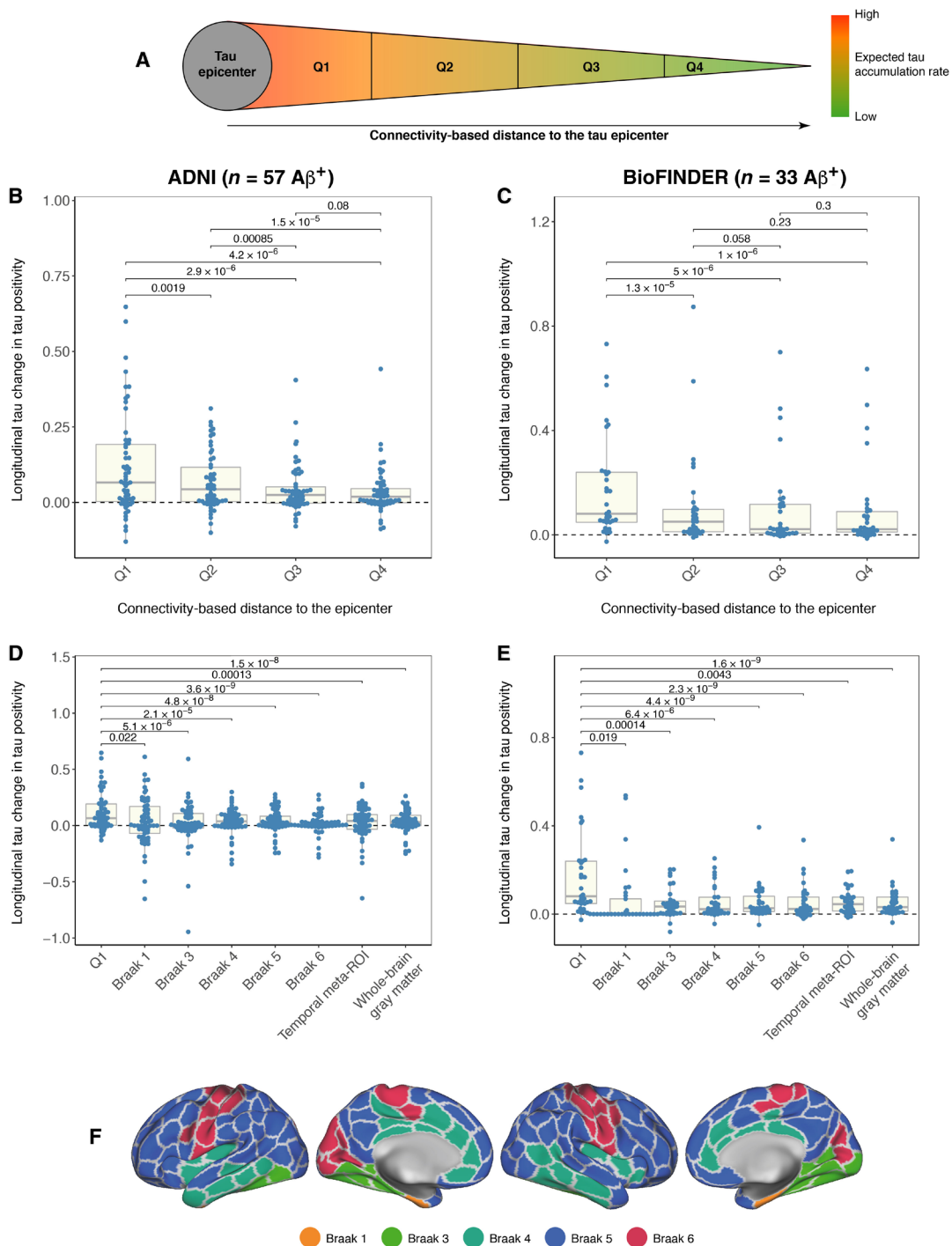
Fig. 6. Subject-specific modeling of longitudinal tau spreading. Using ROI-based tau positivity probabilities, tau epicenters were defined for each subject at baseline, defined as regions with >30% tau positivity probability. We determined for each subject the mean connectivity of tau epicenters and grouped non-epicenter ROIs into quartiles based on the connectivity-based distance to the epicenters (**A**). Note that this determination of Q1 to Q4 ROIs was done for each subject individually based on subject-specific tau epicenters at baseline. For those subjects with evidence of tau epicenters at baseline (i.e., where at least one ROI showed a tau positivity probability of >30%), we determined longitudinal tau changes in quartile distance to the tau epicenters (Q1 in closest connectivity-based proximity to the epicenters versus Q4 in greatest connectivity-based distance to the epicenters). Boxplots show a gradient of tau accumulation from epicenters throughout connected regions (i.e., Q1 to Q4) for ADNI (**B**) and BioFINDER (**C**). Analyses in both ADNI (**D**) and BioFINDER (**E**) show that longitudinal tau change in patient-tailored Q1 ROIs was higher than tau change in Braak stage–specific ROIs [see (**F**)], the temporal meta-ROI [i.e., mean across Braak stages 1, 3, and 4 in (F)], or whole-brain gray matter. All *P* values were determined using paired Wilcoxon tests.

subjects' epicenters) is greater than in Braak stage–specific ROIs, a temporal meta-ROI or whole-brain gray matter ROIs that are agnostic to subject-specific tau epicenters.

Last, we quantified whether using the Q1 ROI predicted by our spreading model (Fig. 6A) is more sensitive as a readout of tau change in tau-targeting trials, as compared to Braak stage–specific, temporal meta-ROI, or whole-brain readouts. To this end, we ran sample size estimations for simulated interventions that reduce longitudinal tau accumulation between 20 and 40% at a statistical power of 80% and an α of 0.05. For all intervention strengths (i.e., 20 to 40%), sample size estimations based on both ADNI and BioFINDER data revealed lowest numbers per arm to detect intervention effects for the Q1 ROI that is predicted by our connectivity-based spreading model compared to Braak stage ROIs 1 to 6, the temporal meta-ROI, or whole-brain gray matter assessments. A detailed summary of estimated subject numbers per treatment arm is provided in Table 2. Together, these findings suggest that using individualized readouts for assessing longitudinal tau changes can substantially enhance the sensitivity to detect longitudinal tau accumulation and increase the sensitivity for detecting tau-targeting intervention effects.

DISCUSSION

The main aim of the current study was to investigate the association between tau spreading patterns and interregional functional connectivity. In two independent samples across the Alzheimer's continuum, we show that cross-sectionally estimated tau spreading sequences follow the normative connectivity pattern of tau epicenters (i.e., those brain regions with the highest likelihood of abnormal tau across $A\beta^+$ subjects). This association was detected not only for AD-typical Braak-like tau spreading patterns, with epicenters mostly located in the inferior temporal lobe, but also for spatially heterogeneous tau-PET subtypes with variable epicenters and tau spreading sequences that occur within the context of the primarily amnestic AD subjects included in the current study. While this result suggests that tau deposition and tau epicenters can be spatially variable, our findings provide evidence that tau pathology emerges locally and spreads subsequently throughout connected regions in AD. This view is also supported by longitudinal tau-PET analyses in $A\beta^+$ subjects: Specifically, we determined subject-specific tau epicenters on baseline tau-PET scans (i.e., defined as regions with highest tau deposition), showing that those regions that were functionally closely connected to the epicenters had the highest future tau accumulation rates. In contrast, regions that were only weakly connected to the epicenters showed slowest future tau accumulation rates. The major novelty of our study is that future tau spreading patterns can be predicted at the individual level based on the normative connectivity patterns of tau epicenters. On the basis of this finding, we propose a patient-tailored method for assessing tau accumulation specifically in those regions that are closely connected to a given patients' tau epicenter. We show that this individualized assessment of tau accumulation can significantly improve the sensitivity to quantify tau accumulation over conventional Braak stage–derived methods that apply the same ROIs across groups of different patients. In simulations, we show that using connectivity-based models to prespecify individualized tau-PET readouts can significantly reduce sample sizes for clinical trials that use longitudinal tau accumulation as a primary end point. Together, the cur-

Table 2. Sample size estimation for detecting tau intervention effects based on different target ROIs.

ADNI:	Target ROI for assessing tau-PET change	Required *n* per arm to detect an intervention effect of		
		20%	30%	40%
	Q1	506	208	109
	Braak 1	766	341	194
	Braak 3	1398	648	382
	Braak 4	732	331	190
	Braak 5	666	294	166
	Braak 6	1121	507	2936
	Temporal meta-ROI	866	396	231
	Whole-brain gray matter	685	306	175
BioFINDER:	Target ROI for assessing tau-PET change	20%	30%	40%
	Q1	395	160	82
	Braak 1	1530	619	318
	Braak 3	463	191	102
	Braak 4	531	216	112
	Braak 5	612	249	129
	Braak 6	615	250	129
	Temporal meta-ROI	484	197	102
	Whole-brain gray matter	470	191	100

rent independently validated results provide further support that tau pathology emerges in local epicenters from where it spreads gradually across connected brain regions in AD. Translating the concept of connectivity-based tau spreading to in vivo tau-PET data is of high clinical importance since connectivity-based tau spreading models may be used for patient-tailored prediction of tau accumulation and disease progression, which may be a critical step forward in establishing precision medicine methods in AD.

We show that the cross-sectionally estimated sequence in which tau spreads across the brain largely follows the functional connectivity pattern of tau epicenters. Tau epicenters are assumed to develop abnormal tau early in the course of AD since these regions show a consistently high likelihood for abnormal tau pathology across CN $A\beta^+$ subjects to AD dementia (28). Our results are broadly consistent with previous work in patients with AD reporting a spatial match between functional connectivity patterns of the entorhinal cortex or inferior temporal brain regions (i.e., epicenters) and group-average Braak-like tau deposition patterns (11, 28, 33). However, our results also show that the AD-typical Braak-like tau spreading scheme assessed in $A\beta^+$ subjects does not fully capture interindividual variability and heterogeneity in tau deposition patterns that were observed in the current sample of presymptomatic or clinically typical (i.e., amnestic) AD. In the ADNI sample of 213 $A\beta^+$ subjects, we show that subjects can be grouped into spatial subtypes of tau deposition (e.g., AD typical, occipital dominant, asymmetric, etc.; see

Figs. 3 to 5), which are characterized by subtype-specific tau epicenters and subtype-specific tau spreading sequences that follow epicenter connectivity. Moreover, connectivity patterns of subtype-specific tau epicenters explained interindividual variability in tau deposition patterns better than the AD-typical Braak-like tau spreading pattern. This finding supports the view that tau deposition can be heterogeneous in AD, which is not always captured by the spatially predefined Braak staging scheme. Our findings suggest that this heterogeneity in tau spreading patterns potentially results from tau starting sites (i.e., epicenters) that can be variable across patients. This interpretation is in line with preclinical studies in tau transgenic mice that use local injections of pathological tau to study tau spreading, showing that the spatial pattern of tau spreading is largely determined by the connectivity pattern of the tau injection site (34, 35). It is, thus, possible that heterogeneous tau deposition patterns, which have been reported in AD variants including posterior cortical atrophy (16), nonamnestic AD, or primary progressive aphasia (14, 17, 18) are driven by variable sites of earliest tau pathology and subsequent spread throughout connected regions. Reasons for spatial variability in earliest tau deposition in patients with AD and, thus, heterogeneous tau spreading patterns may be manifold, including regional differences in gene expression (36, 37), preexisting local brain damage (38), or aberrant local neuronal activity (39). It is important to consider, however, that the current results are restricted to the spatial heterogeneity of tau deposition that occurs across patients with typical (i.e., amnestic) AD that are included in ADNI and BioFINDER. Thus, it will be a critical next step to validate our connectivity-based tau spreading model in clinical AD variants, such as posterior cortical atrophy or nonamnestic AD, to better understand whether and how connectivity may shape the spread of tau in those AD variants that are characterized by highly heterogeneous tau deposition patterns (14). Together, our current findings add to the growing literature showing that tau spreading patterns in AD are closely associated with functional connectivity and the topology of brain networks.

We could extend our cross-sectional results on epicenter connectivity versus estimated tau-spreading sequences in analyses of subject-level longitudinal tau-PET data: Specifically, we defined subject-specific tau epicenters on baseline tau-PET scans as those regions showing highest tau levels and determined the connectivity pattern of each subjects' epicenters to the rest of the brain. When assessing regional tau changes across 1 to 2 years of follow-up, we could show that tau accumulation rates were, in fact, strongest in those brain regions that were in closest connectivity-based proximity to tau epicenters, whereas tau accumulation rates gradually decreased in further connectivity-based distance to the epicenters (illustrated in Fig. 6A). This finding is a critical validation of the cross-sectional association between epicenter connectivity and estimated tau spreading sequences (i.e., for the whole $A\beta^+$ groups or spatial tau subtypes), demonstrating that tau spreads indeed from circumscribed tau epicenters throughout connected regions. In addition, this result is a critical extension of our previous work showing that future tau accumulation of a given brain region can be predicted by baseline tau levels in connected regions (12). Our findings echo previous reports in tau transgenic mice that reported time-dependent tau spreading from local tau injection sites across connected regions (34, 35). Together, these results from preclinical and in vivo tau-PET studies suggest gradual tau accumulation from epicenters across connected regions, thereby providing support for the transneuronal

tau spreading hypothesis (5, 6). However, our findings do not contradict other mechanisms that have been previously linked to the accumulation of tau pathology, including shared vulnerability of brain regions and correlated gene expression among connected regions (36, 40).

Our results are a critical step toward precision medicine, showing that the spatial spread of tau, i.e., the pathological brain change in AD that is most closely linked to cognitive decline and neurodegeneration (41, 42), can be predicted on an individual level. The importance of developing such an individualized tau spreading model is its' potential to inform the assessment of longitudinal tau accumulation, e.g., as an outcome variable in tau-targeting clinical trials where a high sensitivity to detect tau changes is critical for determining treatment effects. Conventional quantitative assessments of longitudinal tau changes may apply the same predefined spatial readout (e.g., Braak stage ROIs, whole brain, or meta-ROIs) across a group of patients (20), which does, however, not take into account spatial heterogeneity in tau accumulation patterns, e.g., across different disease stages or spatial tau subgroups, as reported by us (i.e., Figs. 3 to 5) or others (19–23). Thus, applying the same ROIs as readouts for across subjects with spatially heterogeneous tau accumulation patterns can introduce noise when quantifying longitudinal tau changes, e.g., due to disease stage–specific sensitivity for detecting tau accumulation (20). Our proposed spreading model can address this problem by predefining brain regions with a high likelihood of future tau accumulation in a patient-tailored manner (i.e., Q1 ROI). We demonstrate that this patient-tailored approach (i) significantly improves the ability to quantify longitudinal tau accumulation over assessments in predefined ROIs (i.e., Braak stage specific and whole brain) and (ii) reduces the required sample sizes to detect intervention effects in clinical trials that target tau accumulation. Our prediction model works in a fully automated and data driven manner and can be broadly applied to tau-PET data since it does not require subject-specific connectivity data but builds on a connectivity template assessed on high-quality fMRI data obtained in a normative sample of 1000 healthy individuals. Still, it will be an important next step to test whether the inclusion of high-quality subject-level connectivity data (e.g., based on multi-band resting-state fMRI) may further enhance the prediction of future tau spread since the normative connectivity data used in the current sample does not take into account interindividual connectivity differences or AD-associated connectivity changes that may modulate the spreading of tau (43, 44). Together, our proposed patient-tailored tau spreading model overcomes the limitation of predefined staging methods (i.e., Braak staging), can increase the sensitivity to assess longitudinal tau accumulation, and may thus hold high potential for monitoring tau accumulation and to evaluate the efficacy of treatments that target tau spreading (24, 45).

When interpreting our results, several caveats should be taken into account. First, the AV1451 tau-PET tracer shows considerable unspecific binding in brain regions such as the hippocampus and basal ganglia, which may hamper the modeling of tau spread (30). To address this, we excluded all regions that are severely affected by unspecific binding from the analyses (e.g., hippocampus and basal ganglia). Furthermore, we minimized any influence of AV1451 off-target binding by transforming tau-PET SUVRs to tau positivity probabilities using a Gaussian mixture modeling approach that has been previously applied by amyloid- and tau-PET studies to separate target from unspecific binding (28, 46). Still, it is possible that

unspecific binding influences our results; hence, our results await further replication using second-generation tau-PET data with a better off-target binding profile. Second, partial volume data were only available in BioFINDER, since longitudinal MRI scans matching the longitudinal tau-PET data were only available for a limited number of ADNI subjects. Thus, all results reported are obtained using non–partial volume–corrected data. When repeating all analyses using partial volume–corrected data from BioFINDER, all results remained, however, consistent with the reported results. Furthermore, previous studies using the AV1451 tracer have shown that partial volume correction may enhance the sensitivity to detect tau-PET changes (*20*), but that longitudinal tau-PET changes can also be detected without partial volume correction (*22*, *23*). Thus, we are confident that the results of the current study are not driven by partial volume effects. Third, we would like to acknowledge that the current approach to model tau spreading sequences and subtypes using cross-sectional data is only one of various approaches that have been suggested previously. Notably, previous work has suggested data-driven and event-based models of biomarker changes in AD, which could be readily applied to tau-PET data to estimate tau spreading sequences based on cross-sectional data (*47*, *48*). Second, a more advanced approach has been introduced specifically for neuroimaging data, which is capable of modeling both spatial subtypes and temporal trajectories of pathological brain changes using cross-sectional data (*49*). We believe that these complimentary approaches to determine tau spreading sequences may offer additional opportunities to further validate the association between connectivity and tau spreading in future studies.

In conclusion, the current independently validated results provide clear evidence that tau spreading patterns follow the connectivity pattern of tau epicenters, i.e., regions in which tau potentially emerges first. Our findings are a critical translation of preclinical results (*5*, *7*, *34*) and provide in vivo support for the hypothesis of transneuronal tau spreading in AD (*5*, *6*). Our methodological framework may also be used by future studies to study tau spreading in rare clinical AD variants and non-AD tauopathies, such as progressive supranuclear palsy or corticobasal degeneration, where tau spreading patterns may also be a determined connectivity (*5*, *6*). Our findings a have important clinical implications since connectivity-based modeling of tau spreading may be a promising precision medicine tool to prespecify end points for tau-targeting treatments and to predict future clinical disease progression.

MATERIALS AND METHODS
Sample

Alzheimer's Disease Neuroimaging Initiative
We included a total of 444 subjects from the ADNI database. Inclusion criteria were availability of AV1451 tau-PET, AV45 amyloid-PET, T1 MPRAGE structural MRI, and demographic data. All baseline imaging modalities had to be obtained within a time window of 1.5 years. Each subject Aβ status was determined on the basis of a global AV45 amyloid-PET SUVR normalized to the whole cerebellum using a preestablished FreeSurfer-based protocol using established cut points (global AV45 SUVR of >1.11) (*50*). For an in-depth description of the AV45 amyloid-PET assessment in ADNI, please see https://adni.bitbucket.io/reference/docs/UCBERKELEYAV45/ADNI_AV45_Methods_JagustLab_06.25.15.pdf. For 106 Aβ+ subjects, we additionally included follow-up tau-PET data. Clinical status was assessed by the ADNI investigators, where subjects were categorized as CN [MMSE (Mini Mental State Exam) > 24, CDR (Clinical Dementia Rating) = 0; nondepressed], MCI (MMSE > 24, CDR = 0.5; objective memory impairment on education-adjusted Wechsler Memory Scale II, preserved activities of daily living), or demented (MMSE of 20 to 26, CDR > 0.5; NINCDS/ADRDA criteria for probable AD). Ethical approval was obtained by the ADNI investigators, and all participants provided written informed consent.

BioFINDER
For validation, we included 57 participants from BioFINDER in whom Aβ status, structural MRI, and longitudinal AV1451 tau-PET assessments were available. Aβ status in BioFINDER was determined at baseline using flutemetamol PET, as described previously (*46*), applying a pons-normalized global SUVR cutoff of 0.575 (*51*). In BioFINDER, the Alzheimer's continuum was covered by 16 CN Aβ+, 7 MCI Aβ+, and 18 AD dementia subjects. As a control sample, we included 16 CN Aβ− subjects. Inclusion and exclusion criteria and diagnostic criteria of the BioFINDER study have been described previously (*52*). All participants provided written informed consent to participate in the study before inclusion in the study. Ethical approval was provided by the ethics committee at Lund University, Sweden. Imaging procedures were approved by the Radiation Protection Committee at Skåne University Hospital and by the Swedish Medical Products Agency.

MRI and PET acquisition and preprocessing in ADNI
In ADNI, all MRI data was obtained on 3T scanners with a standardized protocol across sites, where structural MRI was recorded using a three-dimensional (3D) T1-weighted MPRAGE sequence with 1-mm isotropic voxel size (TR = 2300 ms; parameter details can be found on http://adni.loni.usc.edu/wp-content/uploads/2017/07/ADNI3-MRI-protocols.pdf). AV1451 tau-PET was recorded using a standardized protocol using six 5-min time windows 75 to 105 min after intravenous bolus injection of 370-megabecquerel (MBq) radiolabeled ^{18}F-AV1451 tracer. Similarly, AV45 amyloid-PET was recorded in four 5-min time windows 50 to 70 min after intravenous injection of 370-MBq ^{18}F-labeled AV45 tracer. Dynamically acquired images were subsequently realigned and averaged by the ADNI PET core to obtain a single AV1451 or AV45 image and reoriented into a standard 160 × 160 × 96 voxel grid aligned to the anterior commissure–posterior commissure (AC-PC) line to facilitate across site and across scanner comparability. No differences in global tau-PET uptake were found between ADNI sites [analysis of variance (ANOVA); $F = 0.327$, $P = 0.568$], suggesting that there was a site-specific bias in the overall levels of tau-PET. Structural T1 MRI images were normalized to Montreal Neurological Institute (MNI) standard space using Advanced Normalization Tools (ANTs) (*53*). AV1451 and AV45 PET images were then co-registered to the native-space T1 images and subsequently normalized to MNI space by applying the ANTs normalization parameters. From each spatially normalized PET image, we then extracted means of 200 ROIs covering the entire neocortex, using an established brain parcellation (see Fig. 1A) (*31*). To tailor this atlas to the current sample, we additionally masked the ROIs with a group-specific gray matter mask that was binarized at a probability threshold of 0.3.

MRI and PET acquisition and preprocessing in BioFINDER
In BioFINDER, 1-mm isotropic T1-weighted MPRAGE (TR = 1900 ms) and fluid-attenuated inversion recovery (FLAIR; $0.7 \times 0.7 \times 5$ mm^3

of voxel size, 23 slices, TR = 9000 ms) images were acquired for all participants on a 3T Siemens Skyra scanner (Siemens Medical Solutions, Erlangen, Germany). Tau-PET imaging was conducted 80 to 100 min after bolus injection of ^{18}F-flortaucipir on a GE Discovery 690 PET scanner (General Electric Medical Systems, Milwaukee, WI, USA). Radiosynthesis and radiochemical purity for ^{18}F-AV1451 within the BioFINDER study have previously been described in detail (*54*). The image data were processed by the BioFINDER imaging core using a pipeline developed at Lund University that was described previously (*55*). Briefly, the MRIs were skull stripped using the combined MPRAGE and FLAIR data, segmented into gray and white matter, and normalized to MNI space. PET images were attenuation corrected, motion corrected, summed, and coregistered to the MRIs. In line with the ADNI data, SUVR data were calculated using an inferior cerebellar gray matter as a reference region. Usage of an alternative reference region (i.e., eroded white matter) yielded consistent results with the analyses reported in the manuscript. Both non–partial volume–corrected data and data corrected for partial volume using the geometrical transfer matrix method (*56*) were calculated. Usage of partial volume–corrected data yielded consistent findings with the results obtained on non–partial volume–corrected data that are reported in the current manuscript.

Assessment of functional connectivity and connectivity-based distance
To determine a functional connectivity template for the ADNI and BioFINDER sample, we downloaded spatially normalized (i.e., to MNI space) minimally preprocessed 3T resting-state fMRI images from 1000 subjects of the human connectome project (HCP). We further applied detrending, band-pass filtering (0.01 to 0.08 Hz), despiking, and motion correction to the HCP resting-state data. To further eliminate motion artifacts, we performed scrubbing, i.e., removal of high-motion frames, as defined by exceeding 0.5-mm framewise displacement. Specifically, high-motion volumes together with one preceding and two subsequent volumes were replaced with zero-padded volumes to eliminate high-motion volumes but keep the number of volumes consistent across subjects. The 1000 subject-specific functional connectivity matrices were subsequently averaged (Fig. 2I) and thresholded at a density of 30% (Fig. 2J). The resulting thresholded functional connectivity matrix was then converted to distance (i.e., shortest path length between ROIs, Fig. 2K) (*57*). Note that we did not perform global signal regression due to some controversies about potential bias introduced by this preprocessing step (*58*). However, when reanalyzing the data with global signal regression, all results presented in this manuscript remained virtually the same.

Assessment of structural connectivity
Structural connectivity was assessed on the basis of preprocessed diffusion MRI data from 1000 subjects of the human connectome project, corrected for susceptibility-induced B_0 field deviations, eddy current distortions, subject motion, and aligned to native structural space (*59*). To reconstruct the structural connectome, we used a multishell multitissue constrained spherical deconvolution and probabilistic tractography pipeline, as implemented in MRtrix3. This included the following steps: T1-weighted tissue segmentation to generate five tissue-type images, response function estimation ("dhollander" algorithm), estimation of the fiber orientation distribution, multitissue informed log-domain intensity normalization,

modeling 10 million streamlines using anatomically constrained probabilistic streamlines tractography using dynamic seeding and cropping at the GMWM (Grey Matter White Matter) interface, and spherical deconvolution informed filtering of tractograms (SIFT2). Nodes were defined according to the same 200 ROI parcellation used in the functional connectivity template (registered to diffusion space using ANTs). Edges were defined as the SIFT2-filtered number of streamlines. When assigning the streamlines to the nodes, we allowed a radial search of 3 mm and scaled each contribution to the connectome edge by the length of the streamline. Note that the major advantage of SIFT2 filtering is the generation of biologically plausible connectomes where the streamline density in each voxel matches the fiber orientation distribution estimated from the diffusion-weighted images (*60*). From the resulting 1000 structural connectivity matrices, we created the mean to serve as the structural connectivity template.

Transforming tau-PET SUVRs to tau positivity probability
Previous studies have shown that the AV1451 tau-PET tracer shows considerable off-target binding across the brain, causing signal in brain regions that do not harbor pathological tau (*29*). Since our main aim was to model the spread of pathological tau, we adopted a previously described approach that applies Gaussian mixture modeling to PET data to separate target from off-target binding (*28, 46*). The underlying rationale is that most subjects should not show pathological tau in most brain regions; hence, pathological tau-PET signal should show a skewed distribution. In contrast, off-target binding should be unspecific and thus show a normal distribution. A mixture of on-target and off-target signal should thus result in a bimodal distribution that can be separated using Gaussian mixture modeling. To separate on-target from off-target AV1451 signal, we extracted AV1451 tau-PET SUVRs the 200 ROIs included in the brain atlas (Fig. 1) (*31*) and applied Gaussian mixture modeling to ROI-specific tau-PET values across the ADNI or BioFINDER sample. We fitted one- and two-component models and determined the model with the best fit using Akaike's information criterion, revealing a better two-component fit for all 200 ROIs within the ADNI and BioFINDER sample (Fig. 1B). For each subject and ROI, we then determined the probability of falling on the right-most distribution of the two fitted Gaussians. Since this right-most distribution likely reflects abnormal AV1451 tau-PET signal, the probability score expresses the proximity of a subject to the pathological distribution, which can thus be interpreted as a probabilistic measure of tau positivity.

Mapping Braak stages in Schaefer 200 atlas space
To determine tau-PET uptake within Braak stage–specific ROIs, we mapped the Schaefer 200 brain atlas to a previously published Braak staging scheme (*3*). Specifically, we determined for each of the 200 ROIs the maximum spatial overlap with the previously established Braak stage ROIs (*3*), thereby assigning each ROI to a given Braak stage. In line with previous studies, we excluded Braak stage 2 (i.e., hippocampus) because of severe off-target binding within this region.

ICA of tau-PET data
In the large ADNI cohort of 444 subjects, we applied ICA to the spatially normalized voxel-wise tau-PET SUVR data to stratify the sample into spatially heterogeneous subtypes of tau deposition. ICA was performed using the GIFT toolbox in MATLAB (https://trendscenter.org/software/gift/). The number of components to extract was set to 23,

as determined via the minimum description length algorithm. To ensure that the ICA-based clustering of subjects was not driven by disease stage or overall tau levels, the ICA approach included an initial grand mean scaling step so that the spatial pattern of tau-PET and not the absolute tau-PET SUVR was the main determining factor for clustering. To identify AD-related components, we adopted a previously described approach (27) and compared subject-specific component loadings between $A\beta^+$ and $A\beta^-$ groups. ICs with significantly higher loadings in $A\beta^+$ subjects ($P < 0.001$) were identified as AD-related components, and $A\beta^+$ were subsequently assigned to the AD-related components on the basis of maximum component loadings.

Statistics

Within each sample, subject characteristics were compared between groups using chi-square tests for categorical and ANOVAs for numeric variables. All analyses were performed using tau positivity probabilities, which were derived from Gaussian mixture modeling of ROI-specific AV1451 tau-PET SUVR data. We determined cross-sectionally estimated tau spreading sequences for each sample by concatenating ROI-specific tau positivity probabilities across $A\beta^+$ subjects to a 2D matrix. Matrix rows (subjects) and columns (ROIs) were subsequently rank ordered by row and column means, yielding tau spreading matrices (see Fig. 1D). The tau spreading sequence was estimated on the basis of the columns of the tau spreading matrix. Epicenters were defined as those 10% ROIs (i.e., $n = 20$) that showed the earliest tau positivity. Mean connectivity-based distance across the epicenter ROIs was determined on the basis of resting-state fMRI data of the human connectome project. The association between the tau positivity sequence and connectivity-based distance of the epicenters was determined via linear regression. In the $A\beta^+$ subjects of the ADNI sample, we used the same above-described approach to determine tau spreading matrices and the association between estimated tau spreading sequences and epicenter connectivity within the nine IC-defined subtypes of tau pathology. To model subject-specific tau spreading, we used longitudinal data of $A\beta^+$ subjects available in ADNI ($n = 106$) and BioFINDER ($n = 41$). Here, we first determined subject-specific epicenters, defined as ROIs surpassing a tau positivity threshold of 30% at baseline. Subjects without evidence of tau epicenters at baseline (i.e., where none of the 200 ROIs surpassed a baseline tau positivity threshold of 30%) were excluded, leaving a total of $n = 57$ $A\beta^+$ subjects from ADNI and $n = 37$ subjects from BioFINDER for longitudinal analyses. For each remaining subject, we determined mean connectivity-based distance of the subject-specific epicenters based on human connectome project data. Longitudinal change in tau positivity was determined within the epicenter ROIs and in remaining ROIs, grouped into quartiles of connectivity-based distance to the epicenters (i.e., Q1 to Q4; Fig. 6A). In a similar vein, mean longitudinal change in tau positivity was assessed within Braak-specific ROIs and across all 200 ROIs (i.e., whole-brain gray matter). To evaluate whether there was a gradient of tau accumulation from epicenters throughout connected regions, we compared longitudinal tau change between epicenters and Q1 to Q4 ROIs for each sample using paired Wilcoxon tests. To test whether assessing tau change in the patient-tailored Q1 ROI is more sensitive to capture longitudinal tau change than Braak stage–specific or whole-brain gray matter assessments, we compared longitudinal tau changes between subject-specific Q1 ROIs, Braak stage specific, and whole-brain gray matter using

paired Wilcoxon tests. Last, we determined sample size estimates for tau targeting interventions with hypothetical intervention effects of 20/30/40% using the R package pwr (settings: two-sample t test, two-tailed, type I error rate = 0.05, power = 0.8). Analyses were conducted for Q1 and Braak stage specific and whole-brain gray matter.

All statistical analyses were performed in R statistical software. Brain surface renderings were created in connectome workbench. All effects were considered significant at a two-tailed alpha threshold of 0.05.

REFERENCES AND NOTES

1. T. L. S. Benzinger, T. Blazey, C. R. Jack Jr., R. A. Koeppe, Y. Su, C. Xiong, M. E. Raichle, A. Z. Snyder, B. M. Ances, R. J. Bateman, N. J. Cairns, A. M. Faốgan, A. Goate, D. S. Marcus, P. S. Aisen, J. J. Christensen, L. Ercole, R. C. Hornbeck, A. M. Farrar, P. Aldea, M. S. Jasielec, C. J. Owen, X. Xie, R. Mayeux, A. Brickman, E. McDade, W. Klunk, C. A. Mathis, J. Ringman, P. M. Thompson, B. Ghetti, A. J. Saykin, R. A. Sperling, K. A. Johnson, S. Salloway, S. Correia, P. R. Schofield, C. L. Masters, C. Rowe, V. L. Villemagne, R. Martins, S. Ourselin, M. N. Rossor, N. C. Fox, D. M. Cash, M. W. Weiner, D. M. Holtzman, V. D. Buckles, K. Moulder, J. C. Morris, Regional variability of imaging biomarkers in autosomal dominant Alzheimer's disease. *Proc. Natl. Acad. Sci. U.S.A.* **110**, E4502–E4509 (2013).

2. H. Braak, E. Braak, Neuropathological staging of Alzheimer-related changes. *Acta Neuropathol.* **82**, 239–259 (1991).

3. M. Schöll, S. N. Lockhart, D. R. Schonhaut, J. P. O'Neil, M. Janabi, R. Ossenkoppele, S. L. Baker, J. W. Vogel, J. Faria, H. D. Schwimmer, G. D. Rabinovici, W. J. Jagust, PET imaging of tau deposition in the aging human brain. *Neuron* **89**, 971–982 (2016).

4. S. K. Kaufman, K. Del Tredici, T. L. Thomas, H. Braak, M. I. Diamond, Tau seeding activity begins in the transentorhinal/entorhinal regions and anticipates phospho-tau pathology in Alzheimer's disease and PART. *Acta Neuropathol.* **136**, 57–67 (2018).

5. S. Calafate, A. Buist, K. Miskiewicz, V. Vijayan, G. Daneels, B. de Strooper, J. de Wit, P. Verstreken, D. Moechars, Synaptic contacts enhance cell-to-cell tau pathology propagation. *Cell Rep.* **11**, 1176–1183 (2015).

6. A. de Calignon, M. Polydoro, M. Suárez-Calvet, C. William, D. H. Adamowicz, K. J. Kopeikina, R. Pitstick, N. Sahara, K. H. Ashe, G. A. Carlson, T. L. Spires-Jones, B. T. Hyman, Propagation of tau pathology in a model of early Alzheimer's disease. *Neuron* **73**, 685–697 (2012).

7. A. M. Pooler, E. C. Phillips, D. H. W. Lau, W. Noble, D. P. Hanger, Physiological release of endogenous tau is stimulated by neuronal activity. *EMBO Rep.* **14**, 389–394 (2013).

8. R. Ossenkoppele, L. Iaccarino, D. R. Schonhaut, J. A. Brown, J. P. O'Neil, M. Janabi, S. L. Baker, J. H. Kramer, M.-L. Gorno-Tempini, B. L. Miller, H. J. Rosen, W. W. Seeley, W. J. Jagust, G. D. Rabinovici, Tau covariance patterns in Alzheimer's disease patients match intrinsic connectivity networks in the healthy brain. *Neuroimage Clin.* **23**, 101848 (2019).

9. M. C. Hoenig, G. N. Bischof, J. Seemiller, J. Hammes, J. Kukolja, Ö. A. Onur, F. Jessen, K. Fliessbach, B. Neumaier, G. R. Fink, T. van Eimeren, A. Drzezga, Networks of tau distribution in Alzheimer's disease. *Brain* **141**, 568–581 (2018).

10. T. E. Cope, T. Rittman, R. J. Borchert, P. S. Jones, D. Vatansever, K. Allinson, L. Passamonti, P. Vazquez Rodriguez, W. R. Bevan-Jones, J. T. O'Brien, J. B. Rowe, Tau burden and the functional connectome in Alzheimer's disease and progressive supranuclear palsy. *Brain* **141**, 550–567 (2018).

11. N. Franzmeier, A. Rubinski, J. Neitzel, Y. Kim, A. Damm, D. L. Na, H. J. Kim, C. H. Lyoo, H. Cho, S. Finsterwalder, M. Duering, S. W. Seo, M. Ewers; Alzheimer's Disease Neuroimaging Initiative, Functional connectivity associated with tau levels in ageing, Alzheimer's, and small vessel disease. *Brain* **142**, 1093–1107 (2019).

12. N. Franzmeier, J. Neitzel, A. Rubinski, R. Smith, O. Strandberg, R. Ossenkoppele, O. Hansson, M. Ewers; Alzheimer's Disease Neuroimaging Initiative (ADNI), Functional brain architecture is associated with the rate of tau accumulation in Alzheimer's disease. *Nat. Commun.* **11**, 347 (2020).

13. M. E. Murray, N. R. Graff-Radford, O. A. Ross, R. C. Petersen, R. Duara, D. W. Dickson, Neuropathologically defined subtypes of Alzheimer's disease with distinct clinical characteristics: A retrospective study. *Lancet Neurol.* **10**, 785–796 (2011).

14. R. Ossenkoppele, D. R. Schonhaut, M. Schöll, S. N. Lockhart, N. Ayakta, S. L. Baker, J. P. O'Neil, M. Janabi, A. Lazaris, A. Cantwell, J. Vogel, M. Santos, Z. A. Miller, B. M. Bettcher, K. A. Vossel, J. H. Kramer, M. L. Gorno-Tempini, B. L. Miller, W. J. Jagust, G. D. Rabinovici, Tau PET patterns mirror clinical and neuroanatomical variability in Alzheimer's disease. *Brain* **139** (Pt 5), 1551–1567 (2016).

15. R. Ossenkoppele, C. H. Lyoo, C. H. Sudre, D. van Westen, H. Cho, Y. H. Ryu, J. Y. Choi, R. Smith, O. Strandberg, S. Palmqvist, E. Westman, R. Tsai, J. Kramer, A. L. Boxer, M. L. Gorno-Tempini, R. La Joie, B. L. Miller, G. D. Rabinovici, O. Hansson, Distinct tau PET patterns in atrophy-defined subtypes of Alzheimer's disease. *Alzheimers Dement.* **16**, 335–344 (2020).

16. G. S. Day, B. A. Gordon, K. Jackson, J. J. Christensen, M. Rosana Ponisio, Y. Su, B. M. Ances, T. L. S. Benzinger, J. C. Morris, Tau-PET binding distinguishes patients with early-stage posterior cortical atrophy from amnestic Alzheimer disease dementia. *Alzheimer Dis. Assoc. Disord.* **31**, 87–93 (2017).

17. I. M. Nasrallah, Y. J. Chen, M.-K. Hsieh, J. S. Phillips, K. Ternes, G. E. Stockbower, Y. Sheline, C. T. McMillan, M. Grossman, D. A. Wolk, ^{18}F-flortaucipir PET/MRI correlations in nonamnestic and amnestic variants of Alzheimer disease. *J. Nucl. Med.* **59**, 299–306 (2018).

18. K. A. Josephs, P. R. Martin, H. Botha, C. G. Schwarz, J. R. Duffy, H. M. Clark, M. M. Machulda, J. Graff-Radford, S. D. Weigand, M. L. Senjem, R. L. Utianski, D. A. Drubach, B. F. Boeve, D. T. Jones, D. S. Knopman, R. C. Petersen, C. R. Jack Jr., V. J. Lowe, J. L. Whitwell, [^{18}F]AV-1451 tau-PET and primary progressive aphasia. *Ann. Neurol.* **83**, 599–611 (2018).

19. K. Chiotis, L. Saint-Aubert, E. Rodriguez-Vieitez, A. Leuzy, O. Almkvist, I. Savitcheva, M. Jonasson, M. Lubberink, A. Wall, G. Antoni, A. Nordberg, Longitudinal changes of tau PET imaging in relation to hypometabolism in prodromal and Alzheimer's disease dementia. *Mol. Psychiatry* **23**, 1666–1673 (2018).

20. C. R. Jack Jr., H. J. Wiste, C. G. Schwarz, V. J. Lowe, M. L. Senjem, P. Vemuri, S. D. Weigand, T. M. Therneau, D. S. Knopman, J. L. Gunter, D. T. Jones, J. Graff-Radford, K. Kantarci, R. O. Roberts, M. M. Mielke, M. M. Machulda, R. C. Petersen, Longitudinal tau PET in ageing and Alzheimer's disease. *Brain* **141**, 1517–1528 (2018).

21. I. Sintini, P. R. Martin, J. Graff-Radford, M. L. Senjem, C. G. Schwarz, M. M. Machulda, A. J. Spychalla, D. A. Drubach, D. S. Knopman, R. C. Petersen, V. J. Lowe, C. R. Jack Jr., K. A. Josephs, J. L. Whitwell, Longitudinal tau-PET uptake and atrophy in atypical Alzheimer's disease. *Neuroimage Clin.* **23**, 101823 (2019).

22. T. M. Harrison, R. La Joie, A. Maass, S. L. Baker, K. Swinnerton, L. Fenton, T. J. Mellinger, L. Edwards, J. Pham, B. L. Miller, G. D. Rabinovici, W. J. Jagust, Longitudinal tau accumulation and atrophy in aging and alzheimer disease. *Ann. Neurol.* **85**, 229–240 (2019).

23. M. J. Pontecorvo, M. D. Devous, I. Kennedy, M. Navitsky, M. Lu, N. Galante, S. Salloway, P. M. Doraiswamy, S. Southekal, A. K. Arora, A. McGeehan, N. C. Lim, H. Xiong, S. P. Truoccio, A. D. Joshi, S. Shcherbinin, B. Teske, A. S. Fleisher, M. A. Mintun, A multicentre longitudinal study of flortaucipir (^{18}F) in normal ageing, mild cognitive impairment and Alzheimer's disease dementia. *Brain* **142**, 1723–1735 (2019).

24. E. E. Congdon, E. M. Sigurdsson, Tau-targeting therapies for Alzheimer disease. *Nat. Rev. Neurol.* **14**, 399–415 (2018).

25. L. A. Digma, J. R. Madsen, E. T. Reas, A. M. Dale, J. B. Brewer, S. J. Banks; Alzheimer's Disease Neuroimaging Initiative, Tau and atrophy: Domain-specific relationships with cognition. *Alzheimers Res. Ther.* **11**, 65 (2019).

26. R. Ossenkoppele, R. Smith, T. Ohlsson, O. Strandberg, N. Mattsson, P. S. Insel, S. Palmqvist, O. Hansson, Associations between tau, Aβ, and cortical thickness with cognition in Alzheimer disease. *Neurology* **92**, e601–e612 (2019).

27. D. T. Jones, J. Graff-Radford, V. J. Lowe, H. J. Wiste, J. L. Gunter, M. L. Senjem, H. Botha, K. Kantarci, B. F. Boeve, D. S. Knopman, R. C. Petersen, C. R. Jack Jr., Tau, amyloid, and cascading network failure across the Alzheimer's disease spectrum. *Cortex* **97**, 143–159 (2017).

28. J. W. Vogel, Y. Iturria-Medina, O. T. Strandberg, R. Smith, E. Levitis, A. C. Evans, O. Hansson; Alzheimer's Disease Neuroimaging Initiative; Swedish BioFinder Study, Spread of pathological tau proteins through communicating neurons in human Alzheimer's disease. *Nat. Commun.* **11**, 2612 (2020).

29. L. Lemoine, A. Leuzy, K. Chiotis, E. Rodriguez-Vieitez, A. Nordberg, Tau positron emission tomography imaging in tauopathies: The added hurdle of off-target binding. *Alzheimers Dement. (Amst)* **10**, 232–236 (2018).

30. A. Leuzy, K. Chiotis, L. Lemoine, P.-G. Gillberg, O. Almkvist, E. Rodriguez-Vieitez, A. Nordberg, Tau PET imaging in neurodegenerative tauopathies—Still a challenge. *Mol. Psychiatry* **24**, 1112–1134 (2019).

31. A. Schaefer, R. Kong, E. M. Gordon, T. O. Laumann, X.-N. Zuo, A. J. Holmes, S. B. Eickhoff, B. T. T. Yeo, Local-global parcellation of the human cerebral cortex from intrinsic functional connectivity MRI. *Cereb. Cortex* **28**, 3095–3114 (2018).

32. A. Leuzy, R. Smith, R. Ossenkoppele, A. Santillo, E. Borroni, G. Klein, T. Ohlsson, J. Jögi, S. Palmqvist, N. Mattsson-Carlgren, O. Strandberg, E. Stomrud, O. Hansson, Diagnostic

33. J. N. Adams, A. Maass, T. M. Harrison, S. L. Baker, W. J. Jagust, Cortical tau deposition follows patterns of entorhinal functional connectivity in aging. *eLife* **8**, e49132 (2019).

34. Z. Ahmed, J. Cooper, T. K. Murray, K. Garn, E. McNaughton, H. Clarke, S. Parhizkar, M. A. Ward, A. Cavallini, S. Jackson, S. Bose, F. Clavaguera, M. Tolnay, I. Lavenir, M. Goedert, M. L. Hutton, M. J. O'Neill, A novel in vivo model of tau propagation with rapid and progressive neurofibrillary tangle pathology: The pattern of spread is determined by connectivity, not proximity. *Acta Neuropathol.* **127**, 667–683 (2014).

35. M. Iba, J. D. McBride, J. L. Guo, B. Zhang, J. Q. Trojanowski, V. M.-Y. Lee, Tau pathology spread in PS19 tau transgenic mice following locus coeruleus (LC) injections of synthetic tau fibrils is determined by the LC's afferent and efferent connections. *Acta Neuropathol.* **130**, 349–362 (2015).

36. M. J. Grothe, J. Sepulcre, G. Gonzalez-Escamilla, I. Jelistratova, M. Schöll, O. Hansson, S. J. Teipel; Alzheimer's Disease Neuroimaging Initiative, Molecular properties underlying regional vulnerability to Alzheimer's disease pathology. *Brain* **141**, 2755–2771 (2018).

37. J. Sepulcre, M. J. Grothe, F. d'Oleire Uquillas, L. Ortiz-Terán, I. Diez, H.-S. Yang, H. I. L. Jacobs, B. J. Hanseeuw, Q. Li, G. El-Fakhri, R. A. Sperling, K. A. Johnson, Neurogenetic contributions to amyloid beta and tau spreading in the human cortex. *Nat. Med.* **24**, 1910–1918 (2018).

38. R. A. Stern, C. H. Adler, K. Chen, M. Navitsky, J. Luo, D. W. Dodick, M. L. Alosco, Y. Tripodis, D. D. Goradia, B. Martin, D. Mastroeni, N. G. Fritts, J. Jarnagin, M. D. Devous Sr., M. A. Mintun, M. J. Pontecorvo, M. E. Shenton, E. M. Reiman, Tau positron-emission tomography in former national football league players. *N. Engl. J. Med.* **380**, 1716–1725 (2019).

39. X. Y. Tai, M. Koepp, J. S. Duncan, N. Fox, P. Thompson, S. Baxendale, J. Y. W. Liu, C. Reeves, Z. Michalak, M. Thom, Hyperphosphorylated tau in patients with refractory epilepsy correlates with cognitive decline: A study of temporal lobe resections. *Brain* **139** (Pt 9), 2441–2455 (2016).

40. P. E. Vértes, T. Rittman, K. J. Whitaker, R. Romero-Garcia, F. Váša, M. G. Kitzbichler, K. Wagstyl, P. Fonagy, R. J. Dolan, P. B. Jones, I. M. Goodyer; NSPN Consortium, E. T. Bullmore, Gene transcription profiles associated with inter-modular hubs and connection distance in human functional magnetic resonance imaging networks. *Philos. Trans. R. Soc. Lond. B Biol. Sci.* **371**, 20150362 (2016).

41. E. E. Wolters, R. Ossenkoppele, S. C. J. Verfaillie, E. M. Coomans, T. Timmers, D. Visser, H. Tuncel, S. S. V. Golla, A. D. Windhorst, R. Boellaard, W. M. van der Flier, C. E. Teunissen, P. Scheltens, B. N. M. van Berckel, Correction to: Regional [^{18}F]flortaucipir PET is more closely associated with disease severity than CSF p-tau in Alzheimer's disease. *Eur. J. Nucl. Med. Mol. Imaging* **47**, 2934–2935 (2020).

42. R. La Joie, A. V. Visani, S. L. Baker, J. A. Brown, V. Bourakova, J. Cha, K. Chaudhary, L. Edwards, L. Iaccarino, M. Janabi, O. H. Lesman-Segev, Z. A. Miller, D. C. Perry, J. P. O'Neil, J. Pham, J. C. Rojas, H. J. Rosen, W. W. Seeley, R. M. Tsai, B. L. Miller, W. J. Jagust, G. D. Rabinovici, Prospective longitudinal atrophy in Alzheimer's disease correlates with the intensity and topography of baseline tau-PET. *Sci. Transl. Med.* **12**, eaau5732 (2020).

43. J. P. Chhatwal, A. P. Schultz, K. A. Johnson, T. Hedden, S. Jaimes, T. L. S. Benzinger, C. Jack Jr., B. M. Ances, J. M. Ringman, D. S. Marcus, B. Ghetti, M. R. Farlow, A. Danek, J. Levin, I. Yakushev, C. Laske, R. A. Koeppe, D. R. Galasko, C. Xiong, C. L. Masters, P. R. Schofield, K. M. Kinnunen, S. Salloway, R. N. Martins, E. McDade, N. J. Cairns, V. D. Buckles, J. C. Morris, R. Bateman, R. A. Sperling; Dominantly Inherited Alzheimer Network, Preferential degradation of cognitive networks differentiates Alzheimer's disease from ageing. *Brain* **141**, 1486–1500 (2018).

44. N. Franzmeier, E. Düzel, F. Jessen, K. Buerger, J. Levin, M. Duering, M. Dichgans, C. Haass, M. Suárez-Calvet, A. M. Fagan, K. Paumier, T. Benzinger, C. L. Masters, J. C. Morris, R. Perneczky, D. Janowitz, C. Catak, S. Wolfsgruber, M. Wagner, S. Teipel, I. Kilimann, A. Ramirez, M. Rossor, M. Jucker, J. Chhatwal, A. Spottke, H. Boecker, F. Brosseron, P. Falkai, K. Fliessbach, M. T. Heneka, C. Laske, P. Nestor, O. Peters, M. Fuentes, F. Menne, J. Priller, E. J. Spruth, C. Franke, A. Schneider, B. Kofler, C. Westerteicher, O. Speck, J. Wiltfang, C. Bartels, M. A. A. Caballero, D. Metzger, D. Bittner, M. Weiner, J.-H. Lee, S. Salloway, A. Danek, A. Goate, P. R. Schofield, R. J. Bateman, M. Ewers, Left frontal hub connectivity delays cognitive impairment in autosomal-dominant and sporadic Alzheimer's disease. *Brain* **141**, 1186–1200 (2018).

45. S. Jadhav, J. Avila, M. Schöll, G. G. Kovacs, E. Kövari, R. Skrabana, L. D. Evans, E. Kontsekova, B. Malawska, R. de Silva, L. Buee, N. Zilka, A walk through tau therapeutic strategies. *Acta Neuropathol. Commun.* **7**, 22 (2019).

46. S. Palmqvist, H. Zetterberg, K. Blennow, S. Vestberg, U. Andreasson, D. J. Brooks, R. Owenius, D. Hägerström, P. Wollmer, L. Minthon, O. Hansson, Accuracy of brain amyloid detection in clinical practice using cerebrospinal fluid β-amyloid 42: A cross-validation study against amyloid positron emission tomography. *JAMA Neurol.* **71**, 1282–1289 (2014).

performance of RO948 F 18 tau positron emission tomography in the differentiation of Alzheimer disease from other neurodegenerative disorders. *JAMA Neurol.* **77**, 955–965 (2020).

47. A. L. Young, N. P. Oxtoby, P. Daga, D. M. Cash, N. C. Fox, S. Ourselin, J. M. Schott, D. C. Alexander; Alzheimer's Disease Neuroimaging Initiative, A data-driven model of biomarker changes in sporadic Alzheimer's disease. *Brain* **137** (Pt 9), 2564–2577 (2014).

48. R. V. Marinescu, A. Eshaghi, M. Lorenzi, A. L. Young, N. P. Oxtoby, S. Garbarino, S. J. Crutch, D. C. Alexander; Alzheimer's Disease Neuroimaging Initiative, DIVE: A spatiotemporal progression model of brain pathology in neurodegenerative disorders. *Neuroimage* **192**, 166–177 (2019).

49. A. L. Young, R. V. Marinescu, N. P. Oxtoby, M. Bocchetta, K. Yong, N. C. Firth, D. M. Cash, D. L. Thomas, K. M. Dick, J. Cardoso, J. van Swieten, B. Borroni, D. Galimberti, M. Masellis, M. C. Tartaglia, J. B. Rowe, C. Graff, F. Tagliavini, G. B. Frisoni, R. Laforce Jr., E. Finger, A. de Mendonça, S. Sorbi, J. D. Warren, S. Crutch, N. C. Fox, S. Ourselin, J. M. Schott, J. D. Rohrer, D. C. Alexander; The Genetic FTD Initiative (GENFI); The Alzheimer's Disease Neuroimaging Initiative (ADNI), Uncovering the heterogeneity and temporal complexity of neurodegenerative diseases with subtype and stage inference. *Nat. Commun.* **9**, 4273 (2018).

50. S. M. Landau, M. A. Mintun, A. D. Joshi, R. A. Koeppe, R. C. Petersen, P. S. Aisen, M. W. Weiner, W. J. Jagust; Alzheimer's Disease Neuroimaging Initiative, Amyloid deposition, hypometabolism, and longitudinal cognitive decline. *Ann. Neurol.* **72**, 578–586 (2012).

51. L. Thurfjell, J. Lilja, R. Lundqvist, C. Buckley, A. Smith, R. Vandenberghe, P. Sherwin, Automated quantification of ^{18}F-flutemetamol PET activity for categorizing scans as negative or positive for brain amyloid: Concordance with visual image reads. *J. Nucl. Med.* **55**, 1623–1628 (2014).

52. N. Mattsson, R. Smith, O. Strandberg, S. Palmqvist, M. Schöll, P. S. Insel, D. Hagerstrom, T. Ohlsson, H. Zetterberg, K. Blennow, J. Jögi, O. Hansson, Comparing ^{18}F-AV-1451 with CSF t-tau and p-tau for diagnosis of Alzheimer disease. *Neurology* **90**, e388–e395 (2018).

53. B. B. Avants, N. J. Tustison, G. Song, P. A. Cook, A. Klein, J. C. Gee, A reproducible evaluation of ANTs similarity metric performance in brain image registration. *Neuroimage* **54**, 2033–2044 (2011).

54. A. Hahn, M. Schain, M. Erlandsson, P. Sjölin, G. M. James, O. T. Strandberg, D. Hägerström, R. Lanzenberger, J. Jögi, T. G. Olsson, R. Smith, O. Hansson, Modeling strategies for quantification of in vivo ^{18}F-AV-1451 binding in patients with tau pathology. *J. Nucl. Med.* **58**, 623–631 (2017).

55. R. Smith, A. Puschmann, M. Schöll, T. Ohlsson, J. van Swieten, M. Honer, E. Englund, O. Hansson, ^{18}F-AV-1451 tau PET imaging correlates strongly with tau neuropathology in *MAPT* mutation carriers. *Brain* **139** (Pt 9), 2372–2379 (2016).

56. O. G. Rousset, Y. Ma, A. C. Evans, Correction for partial volume effects in PET: Principle and validation. *J. Nucl. Med.* **39**, 904–911 (1998).

57. M. Rubinov, O. Sporns, Complex network measures of brain connectivity: Uses and interpretations. *Neuroimage* **52**, 1059–1069 (2010).

58. K. Murphy, M. D. Fox, Towards a consensus regarding global signal regression for resting state functional connectivity MRI. *Neuroimage* **154**, 169–173 (2016).

59. M. F. Glasser, S. N. Sotiropoulos, J. A. Wilson, T. S. Coalson, B. Fischl, J. L. Andersson, J. Xu, S. Jbabdi, M. Webster, J. R. Polimeni, D. C. Van Essen, M. Jenkinson; WU-Minn HCP Consortium, The minimal preprocessing pipelines for the human connectome project. *Neuroimage* **80**, 105–124 (2013).

60. R. E. Smith, J.-D. Tournier, F. Calamante, A. Connelly, SIFT2: Enabling dense quantitative assessment of brain white matter connectivity using streamlines tractography. *Neuroimage* **119**, 338–351 (2015).